ARTICLES
https://doi.org/10.1038/s41590-022-01285-0
nature immunology

Check for updates

ETS1 governs pathological tissue-remodeling programs in disease-associated fibroblasts

Minglu Yan[1], Noriko Komatsu[1], Ryunosuke Muro[1], Nam Cong-Nhat Huynh[1,2], Yoshihiko Tomofuji[3], Yukinori Okada[3,4,5], Hiroshi I. Suzuki[6,7], Hiroyuki Takaba[1], Riko Kitazawa[8], Sohei Kitazawa[9], Warunee Pluemsakunthai[1], Yuichi Mitsui[10,11], Takashi Satoh[10,11], Tadashi Okamura[12], Takeshi Nitta[1], Sin-Hyeog Im[13,14,15], Chan Johng Kim[13], George Kollias[16,17], Sakae Tanaka[18], Kazuo Okamoto[19], Masayuki Tsukasaki[1] and Hiroshi Takayanagi[1]✉

Fibroblasts, the most abundant structural cells, exert homeostatic functions but also drive disease pathogenesis. Single-cell technologies have illuminated the shared characteristics of pathogenic fibroblasts in multiple diseases including autoimmune arthritis, cancer and inflammatory colitis. However, the molecular mechanisms underlying the disease-associated fibroblast phenotypes remain largely unclear. Here, we identify ETS1 as the key transcription factor governing the pathological tissue-remodeling programs in fibroblasts. In arthritis, ETS1 drives polarization toward tissue-destructive fibroblasts by orchestrating hitherto undescribed regulatory elements of the osteoclast differentiation factor receptor activator of nuclear factor-κB ligand (RANKL) as well as matrix metalloproteinases. Fibroblast-specific ETS1 deletion resulted in ameliorated bone and cartilage damage under arthritic conditions without affecting the inflammation level. Cross-tissue fibroblast single-cell data analyses and genetic loss-of-function experiments lent support to the notion that ETS1 defines the perturbation-specific fibroblasts shared among various disease settings. These findings provide a mechanistic basis for pathogenic fibroblast polarization and have important therapeutic implications.

Since they were first described by Virchow[1], fibroblasts have long been regarded as featureless stromal cells with a spindle morphology. However, recent progress in single-cell RNA-sequencing (scRNA-seq) technologies unveiled the amazing diversity and crucial roles of fibroblast functions in health and disease[2–5]. Cross-disease and pan-tissue single-cell approaches illustrate the emerging concept that 'universal fibroblast', a common ancestry of fibroblast subtypes across various organs, acquires shared pathogenic activation states in multiple diseases such as arthritis, cancer and colitis[4,6]. Two major pathogenic fibroblast populations, pro-inflammatory (or immune-interacting) and tissue-destructive (or tissue-remodeling) fibroblasts, are commonly found across diseases[3–5]; hence, there may exist a shared regulatory system underlying the pathogenic fibroblast polarization[7], but this mechanism has never been identified.

Synovial fibroblasts (SFs) are the major component cells of the synovium, providing a structural framework as well as lubrication for joint homeostasis[3]. We proposed the pathological importance of SFs in the bone destruction that occurs in arthritis and showed RANKL to be one of the critical factors responsible for this tissue damage[8–13]. Recent studies using scRNA-seq analyses and transfer experiments demonstrated that SFs critically contribute to the pathogenesis of rheumatoid arthritis (RA) by acquiring either a pro-inflammatory or a tissue-destructive phenotype via unknown mechanisms[14]. The tissue-destructive fibroblasts produce RANKL and matrix metalloproteinases (MMPs) that induce osteoclastic bone destruction and enzymatic cartilage degradation, respectively[14]. However, it is unknown what drives the polarization toward tissue-destructive fibroblasts under arthritic conditions.

Here, we analyzed the transcriptional network and the chromatin landscape of SFs derived from individuals with arthritis and mice, showing that ETS1 choreographs a tissue-destructive gene program in arthritic SFs. Single-cell data analyses across diseases further suggested that the ETS1 expression is also associated with pathogenic fibroblast phenotypes in colitis and cancer. Thus, ETS1-centered transcriptional machinery in fibroblasts crucially contributes to the

[1]Department of Immunology, Graduate School of Medicine and Faculty of Medicine, The University of Tokyo, Tokyo, Japan. [2]Laboratory of Oral-Maxillofacial Biology, Faculty of Odonto-Stomatology, University of Medicine and Pharmacy at Ho Chi Minh City, Ho Chi Minh City, Vietnam. [3]Department of Statistical Genetics, Osaka University, Graduate School of Medicine, Osaka, Japan. [4]Department of Genome Informatics, Graduate School of Medicine, The University of Tokyo, Tokyo, Japan. [5]Laboratory for Systems Genetics, RIKEN Center for Integrative Medical Sciences, Kanagawa, Japan. [6]Division of Molecular Oncology, Center for Neurological Diseases and Cancer, Nagoya University Graduate School of Medicine, Nagoya, Japan. [7]Institute for Glyco-core Research (iGCORE), Nagoya University, Nagoya, Japan. [8]Division of Diagnostic Pathology, Ehime University Hospital, Toon City, Japan. [9]Department of Molecular Pathology, Graduate School of Medicine, Ehime University, Toon City, Japan. [10]Department of Immune Regulation, Graduate School of Medical and Dental Sciences, Tokyo Medical and Dental University, Tokyo, Japan. [11]Innate Cell Therapy, Osaka, Japan. [12]Department of Laboratory Animal Medicine, Research Institute, National Center for Global Health and Medicine, Tokyo, Japan. [13]Department of Life Sciences, Pohang University of Science and Technology (POSTECH), POSTECH Biotech Center, Pohang, Republic of Korea. [14]ImmunoBiome, Pohang, Republic of Korea. [15]Institute of Convergence Science, Yonsei University, Seoul, Republic of Korea. [16]Institute for Bioinnovation, Biomedical Sciences Research Center (BSRC) 'Alexander Fleming,' Vari, Attika, Greece. [17]Department of Physiology, Medical School, National and Kapodistrian University of Athens, Athens, Greece. [18]Department of Orthopaedic Surgery, Faculty of Medicine, The University of Tokyo, Tokyo, Japan. [19]Department of Osteoimmunology, Graduate School of Medicine and Faculty of Medicine, The University of Tokyo, Tokyo, Japan. ✉e-mail: takayana@m.u-tokyo.ac.jp

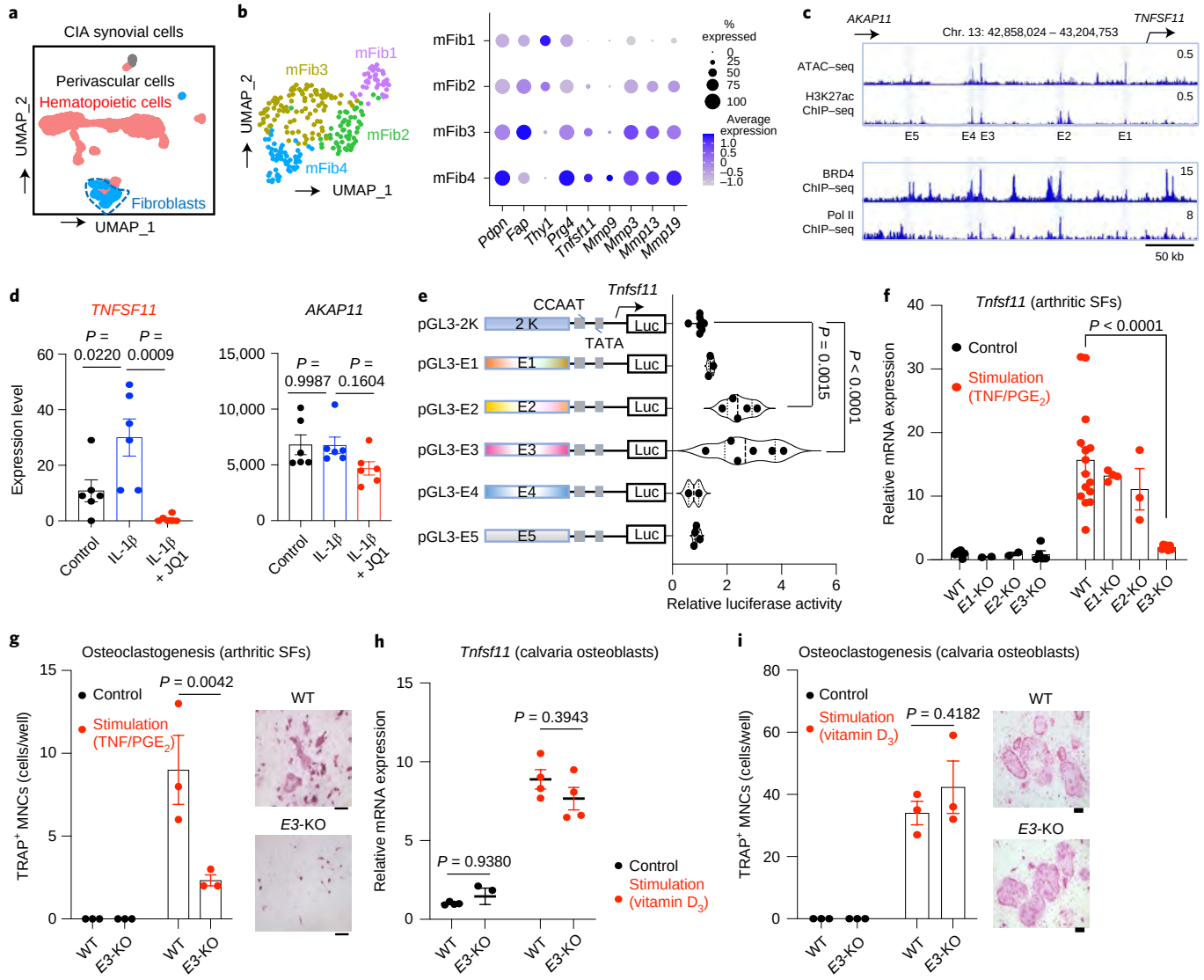

Fig. 1 | A distal enhancer element regulates RANKL gene expression in arthritic synovial fibroblasts. a, Uniform manifold approximation and projection (UMAP) plot of synovial cells ($n = 2{,}160$) from CIA mice ($n = 3$) and untreated control mice ($n = 9$) colored by cluster. **b**, Unsupervised clustering of fibroblasts (mFib1–mFib4) indicated by color (left). Dot plot (right) showing the expression of selected genes in the identified SF clusters. **c**, Epigenomic analyses of RA SFs by ATAC-seq (GSE128644), H3K27ac ChIP-seq (GSE128642), BRD4 and Pol II ChIP-seq (GSE148399). **d**, The *TNFSF11* and *AKAP11* expression levels in RA SFs treated with or without IL-1β and JQ1 ($n = 6$ per group; GSE148395). **e**, Reporter assay for the measurement of mouse E1–E5 enhancer activity for RANKL gene transcription. Individual enhancer activity was assessed by relative luciferase expression in comparison with the *Tnfsf11* promoter vector pGL3-2K[57], $n = 8, 3, 5, 6, 2$ and 4. **f**, *Tnfsf11* mRNA expression in the arthritic SFs derived from WT and enhancer-KO mice (WT, $n = 8$ (control) and $n = 15$ (stimulation); *E1*-KO, $n = 2$ (control) and $n = 4$ (stimulation); *E2*-KO, $n = 2$ (control) and $n = 3$ (stimulation); *E3*-KO, $n = 5$ (control) and $n = 7$ (stimulation)). **g**, Osteoclast formation after the co-culture of bone marrow cells with arthritic SFs of WT or *E3*-KO mice ($n = 3$ per group). The number of TRAP$^+$ multinucleated cells (more than three nuclei; MNCs) is shown. Scale bar, 100 μm. **h**, *Tnfsf11* mRNA in osteoblasts derived from WT and *E3*-KO mice (WT, $n = 4$ (control) and $n = 4$ (stimulation); E3-KO, $n = 3$ (control) and $n = 4$ (stimulation)). **i**, Osteoclast formation after the co-culture of bone marrow cells with neonatal calvaria osteoblasts of WT or *E3*-KO mice ($n = 3$). The number of TRAP$^+$ MNCs is shown. Scale bar, 100 μm. Data are the mean ± s.e.m, (**d**, **f**, **g** (left), **h** and **i** (left)). *P* values were determined by one-way analysis of variance (ANOVA; **d** and **e**) and two-way ANOVA (**f** and **h**) followed by Tukey's post hoc test. In **g** and **i**, *P* values were determined by two-way ANOVA analysis followed by Sidak's multiple-comparisons test.

RA pathogenesis and may represent a shared mechanism regulating fibroblast pathogenicity in multiple diseases.

Results

Characterization of destructive fibroblasts in arthritis. A previous report identified tissue-destructive fibroblasts that express both RANKL and MMPs in a murine serum transfer-induced arthritis (STIA) model in which the activation of the adaptive immune system is bypassed[14]. To test whether the concept of tissue-destructive fibroblasts is generalized to autoimmune arthritis, we performed scRNA-seq of synovial cells derived from collagen-induced arthritis (CIA) mice and analyzed two publicly available scRNA-seq datasets of individuals with RA[15,16].

Unsupervised clustering of our scRNA-seq data of CIA synovial cells identified three major populations: hematopoietic cells, fibroblasts and perivascular cells (Fig. 1a and Extended Data Fig. 1a). Sub-clustering analysis on the fibroblast population showed that the murine arthritic fibroblasts were subdivided

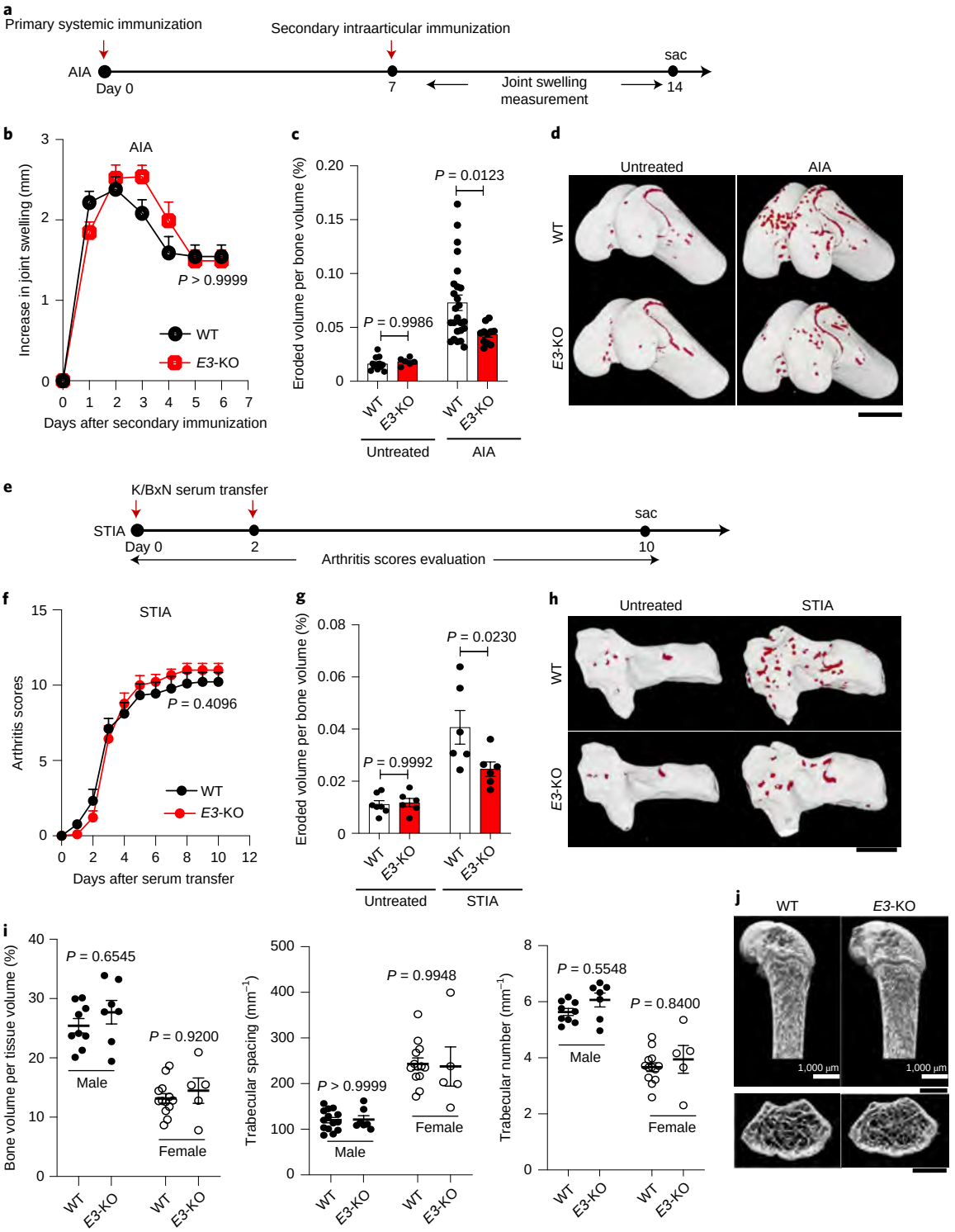

Fig. 2 | *E3* deletion ameliorates arthritis-induced bone damage. a, Schematic showing the murine AIA model. **b**, Joint swelling in WT and *E3*-KO mice ($n=11$ per group) under the AIA condition. *P* values were determined by two-tailed Mann–Whitney *U* test. **c**, Eroded volume per bone volume of the knee joint in WT mice (untreated, $n=12$; AIA, $n=25$) and *E3*-KO mice (untreated, $n=6$; AIA, $n=11$) analyzed by micro-CT. **d**, Representative micro-CT images of the femurs of WT and *E3*-KO mice under untreated and AIA conditions. The red area indicates the erosive cavities evaluated by micro-CT analysis. Scale bars, 1 mm. **e**, Schematic showing murine STIA model. **f**, Arthritis scores of WT and *E3*-KO mice ($n=9$ per group) under STIA condition. *P* values were determined by two-tailed Mann–Whitney *U* test. **g**, Eroded volume per bone volume of the ankle joints in WT mice (untreated, $n=7$; STIA, $n=6$) and *E3*-KO mice (untreated, $n=6$; STIA, $n=6$) analyzed by micro-CT. **h**, Representative micro-CT images of the ankles of WT and *E3*-KO mice under untreated and STIA conditions. The red area indicates the erosive cavities evaluated by micro-CT analysis. Scale bars, 1 mm. **i**, Micro-CT analysis of bone volume per tissue volume, trabecular spacing and number of WT mice (male, $n=9$; female, $n=13$) and *E3*-KO mice (male, $n=7$; female, $n=5$) at the age of 10 weeks under physiological conditions. **j**, Representative micro-CT images of the femurs of WT and *E3*-KO male mice (10 weeks); micro-CT scale bars, 1 mm. Data are the mean ± s.e.m, (**b**, **c**, **f**, **g** and **i**). *P* values were determined by two-way ANOVA analysis followed by Tukey's post hoc test (**c**, **g** and **i**).

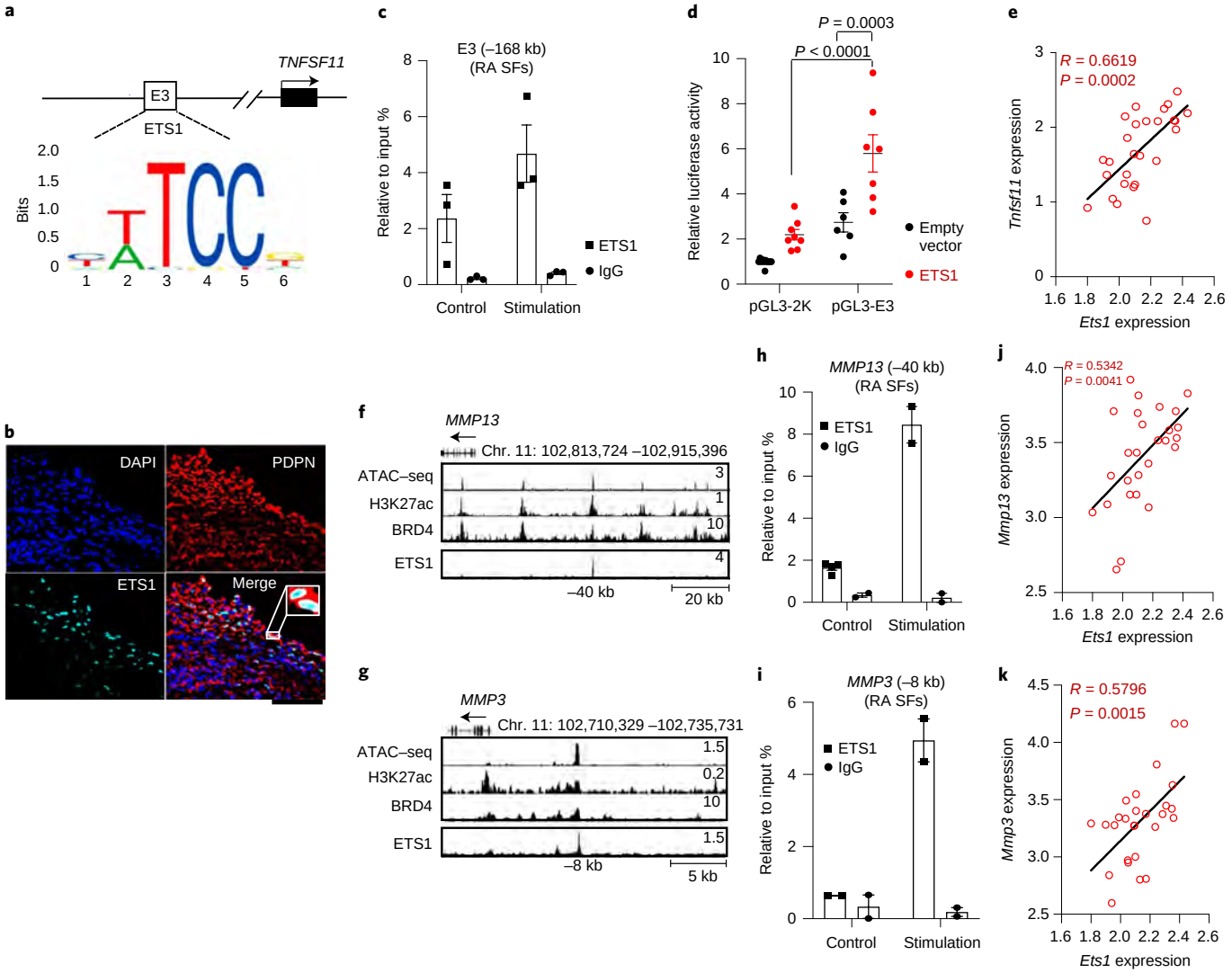

Fig. 3 | Transcriptional regulation of tissue-destructive genes by ETS1. a, Schematic depicting the E3 region upstream of the *TNFSF11* transcription start site (TSS; 168 kb upstream) and enriched ETS1 binding motifs (Jaspar, MA0098.1). **b**, Representative immunofluorescence images of the synovial tissue of individuals with RA ($n=4$). Scale bar, 100 μm. **c**, ChIP of ETS1 binding in the E3 region analyzed by quantitative PCR in SFs from individuals with RA ($n=3$). Data are expressed as the mean ± s.e.m. **d**, Reporter assay for the measurement of pGL3-2K and pGL3-E3 for RANKL gene transcription in the presence of expression vector for ETS1. pGL3-2K, $n=11$ (empty vector) and $n=8$ (ETS1 expression vector) of biologically independent samples. pGL3-E3, $n=6$ (empty vector) and $n=7$ (ETS1 expression vector) of biologically independent samples. Data are expressed as the mean ± s.e.m. *P* values were determined by two-way ANOVA analysis followed by Tukey's post hoc test. **e**, Correlation analysis (Pearson *R* and two-tailed *P* value) between *Ets1* expression and *Tnfsf11* expression in arthritic SFs isolated from STIA mice (GSE129451), $n=27$. **f**,**g**, ATAC-seq (GSE128644), H3K27ac ChIP-seq (GSE128642) and BRD4 ChIP-seq (GSE148399) analyses of SFs from individuals with RA at the *MMP13* locus (**f**) and *MMP3* locus (**g**), and the representative ETS1 ChIP-seq (ENCFF614VLL) in lung fibroblasts from the ENCODE Project database. The ETS1-bound regions are highlighted in gray. **h**,**i**, ChIP of ETS1 binding at the −40-kb region of the *MMP13* locus (**h**; control, ETS1 $n=4$ and IgG $n=2$; stimulation, $n=2$ and −8-kb region of the *MMP3* locus (**i**; $n=2$) analyzed by quantitative PCR in SFs from individuals with RA. Data are expressed as the mean ± s.e.m. **j**,**k**, Correlation analysis (Pearson *R* and two-tailed *P* value) between *Ets1* expression and *Mmp13* (**j**) *and Mmp3* (**k**) expression in arthritic SFs isolated from STIA mice (GSE129451; $n=27$).

into four clusters (Fig. 1b; hereafter referred to as mFib1–4). We found that RANKL (encoded by *Tnfsf11*) and MMPs were highly expressed in fibroblast cluster mFib4 (Fig. 1b), suggesting that this population represents the tissue-destructive fibroblasts in a CIA model. To explore their counterparts in human arthritic synovium, we integrated the two scRNA-seq datasets of SFs from individuals with RA and found that the fibroblast cluster F3 exhibited a high expression level of RANKL and MMPs, indicating that the cluster F3 comprised tissue-destructive fibroblasts in human RA synovium (Extended Data Fig. 1b–d). These data suggested that the presence of tissue-destructive fibroblasts expressing both RANKL and MMPs is a shared feature of the arthritic synovium among murine arthritis models and individuals with RA.

A distal enhancer controls RANKL expression in arthritic synovial fibroblasts. Although it is well established that arthritis-induced bone destruction is caused by the RANKL derived from SFs[8,9,12,14], the molecular mechanisms regulating RANKL gene expression in SFs remain largely unknown. In other cell types, such as osteoblasts and lymphocytes, RANKL gene expression is tightly controlled by transcription factors that act on distal enhancer elements[17,18]. We analyzed epigenomic data of SFs derived from individuals with

RA (GSE128642, GSE128644 and GSE148399)[19,20], focusing on the *TNFSF11* locus. Assays for transposase-accessible chromatin with sequencing (ATAC–seq) and chromatin immunoprecipitation followed by sequencing (ChIP–seq) along with an antibody to acetylated histone H3 Lys27 (H3K27ac) identified five chromatin accessible regions with an enrichment of enhancer marker H3K27ac (the five regions hereafter referred to as E1 to E5) upstream of the *TNFSF11* locus (Fig. 1c). Among the five regions, E2 and E3 were co-occupied by bromodomain protein BRD4 and RNA polymerase II (Pol II; Fig. 1c), indicating that E2 and E3 represent active enhancers in arthritic SFs. Treatment with a small-molecule bromodomain inhibitor, JQ1, markedly repressed the expression levels of *TNFSF11* in RA SFs, without influencing the expression of the adjacent *AKAP11* gene (Fig. 1d), suggesting that these enhancers may play a role specifically in RANKL regulation in SFs.

The E1–E5 sequences are highly conserved among vertebrates (Extended Data Fig. 1e) and the homologous regions of E1, E2 and E3 in mice harbor a similar epigenomic feature in arthritic SFs (Extended Data Fig. 1f). We performed an enhancer reporter assay[21] to identify the enhancer element responsible for RANKL expression in arthritic SFs. Among the five enhancer elements, E3 displayed the strongest capacity to induce RANKL promoter activity (Fig. 1e). It should be noted that the E3 region was inactive in other cell types (Extended Data Fig. 1f) and has never been previously reported as a regulatory element controlling RANKL expression. We found that E2, a previously reported RANKL enhancer in osteoblasts[18] (Extended Data Fig. 1f), also positively regulated RANKL promoter activity, albeit to a lesser extent than E3 (Fig. 1e).

To examine the role of these enhancer elements in vivo, we generated mice lacking E1, E2 or E3. We tested antigen-induced arthritis (AIA)[22,23] in each knockout (KO) strain and found that the RANKL expression in SFs was markedly decreased in the *E3*-KO mice under an inflammatory microenvironment (Fig. 1f and Extended Data Fig. 1g). Deletion of E1 or E2 did not affect the arthritis-induced RANKL expression in the SFs (Fig. 1f).

In vitro co-culture of wild-type (WT) SFs with bone marrow cells generated osteoclasts upon inflammatory stimulation, whereas *E3*-KO SFs failed to support osteoclast formation (Fig. 1g). On the other hand, the RANKL expression in osteoblasts and lymphocytes was normal in the *E3*-KO mice (Fig. 1h and Extended Data Fig. 1h), and the capacity to support osteoclastogenesis was not affected in *E3*-KO osteoblasts (Fig. 1i).

To determine the functional relevance of the E3 enhancer in arthritis-induced bone destruction, we induced AIA and STIA[14,22] on *E3*-KO mice. There was no difference between the WT and *E3*-KO mice in terms of joint swelling and arthritis scores under AIA and STIA conditions (Fig. 2a–f). The synovial cell number and cellular composition were comparable in WT and *E3*-KO arthritis mice (Extended Data Fig. 2a–c). Notably, the *E3*-KO mice exhibited reduced arthritis-associated bone erosion in comparison with WT mice (Fig. 2c,d,g,h). However, the *E3*-KO mice displayed a normal bone phenotype in the steady state (Fig. 2i,j), indicating that E3 was not required for physiological bone remodeling. These findings suggest that the distal enhancer E3 critically contributes to arthritis-induced bone destruction by regulating RANKL expression in SFs.

ETS1 transcriptionally regulates destructive genes in synovial fibroblasts. We next explored the transcription regulator that controls E3 activity. Motif enrichment analysis suggested that ETS transcription factor binding motifs were highly enriched in the E3 region (Fig. 3a and Extended Data Fig. 3a). Among the 27 ETS members, ETS1 showed the highest gene expression levels in SFs derived from individuals with RA (Extended Data Fig. 3b). ETS1 expression in arthritic SFs was significantly induced by tumor necrosis factor (TNF) stimulation and was markedly increased by treatment with the combination of TNF and seven other pro-inflammatory cytokines (interleukin (IL)-1β, IL-6, IL-17, IL-18, interferon (IFN)-γ, IFN-α and transforming growth factor (TGF)-β1; Extended Data Fig. 3b), a condition which mimics the arthritic synovial milieu[24]. The scRNA-seq data analyses revealed that ETS1 is predominantly expressed in the tissue-destructive fibroblast clusters, F3 in the human RA synovium (Extended Data Figs. 1d and 3c) and mFib4 in a CIA model (Fig. 1b and Extended Data Fig. 3d). Motif gene-set enrichment analysis showed that tissue-destructive fibroblasts highly express genes regulated by ETS1 (Extended Data Fig. 3e), suggesting that the ETS1-centered transcriptional program is active in these cells. We confirmed that ETS1 is highly expressed in the SFs of individuals with RA at the protein level (Fig. 3b).

ETS1 is a key transcription factor in the development and function of immune and endothelial cells[25,26], but its role in fibroblasts remains poorly understood. A trans-ethnic genome-wide association study (GWAS) revealed an association of *ETS1* gene variants with RA susceptibility[27]. We found that the GWAS variants localized to the enhancer-like regions in the SFs derived from individuals with RA (Extended Data Fig. 3f), suggesting that the ETS1 dysregulation in SFs may contribute to RA pathogenesis.

We performed ChIP analysis on SFs from individuals with RA and found that ETS1 binds to the E3 RANKL enhancer region (Fig. 3c). Consistent with the previous reports, stimulation with inflammatory cytokines enhanced the DNA binding activity of ETS1 (refs. [28,29]; Fig. 3c). An enhancer reporter assay showed that ETS1 markedly augmented E3 enhancer activity (Fig. 3d). These results suggest that ETS1 has the capacity to stimulate RANKL expression in SFs by binding to the E3 region. We confirmed that the expression level of *Ets1* positively correlated with that of *Tnfsf11* in arthritic SFs (Fig. 3e).

Does ETS1 also control cartilage-degrading enzyme genes in addition to RANKL? A previous report showed that tissue-destructive fibroblasts highly express MMP13 and MMP3 and contribute to cartilage damage in a murine arthritis model[14]. Analysis of ATAC–seq and H3K27ac, BRD4 ChIP–seq data of arthritic SFs suggested the presence of active enhancer elements upstream of the *MMP13* and *MMP3* loci (Fig. 3f,g). Inspection of the ETS1 ChIP–seq data from the Encyclopedia of DNA Elements (ENCODE) Project database suggested that these *MMP13* and *MMP3* enhancers were potentially bound by ETS1 in fibroblasts (Fig. 3f,g). We further confirmed the ETS1 binding to these enhancers by performing ChIP analyses using SFs from individuals with RA (Fig. 3h,i). The expression levels of *Mmp13* and *Mmp3* positively correlated with the *Ets1* expression in arthritic SFs (Fig. 3j,k). Collectively, these results suggest that ETS1 has the capacity to induce both bone-damaging and cartilage-damaging factors through distal enhancer regulation in arthritic SFs.

***Ets1* deletion in synovial fibroblasts attenuates arthritic joint destruction.** To examine the role of *Ets1* expressed in SFs in vivo, we crossed *Ets1*-floxed ($Ets1^{flox}$)[30] mice with *Col6a1*-Cre mice[31] in which Cre recombinase is specifically expressed in SFs in the skeletal system[8,9,31,32]. Our scRNA-seq data confirmed that the *Col6a1* expression was restricted to the fibroblast population within the synovium and there was no difference in *Col6a1* expression between inflammatory (cluster mFib1) and tissue-destructive (cluster mFib4) fibroblasts (Extended Data Fig. 4a,b). We confirmed the specific *Ets1* deletion in SFs in $Ets1^{flox/flox}$ *Col6a1*-Cre mice (hereafter referred to as $Ets1^{\Delta Fib}$; Extended Data Fig. 4c). $Ets1^{\Delta Fib}$ mice grew normally and displayed no abnormalities in the bone structure in the steady state compared with the control $Ets1^{flox}$ mice (Extended Data Fig. 4d,e). Next, we induced STIA[14,22] on $Ets1^{\Delta Fib}$ mice. There was no difference between $Ets1^{flox}$ and $Ets1^{\Delta Fib}$ mice in terms of the joint inflammation or immune cell infiltration into the synovial tissue (Fig. 4a,b and Extended Data Fig. 4f,g). Notably, micro-computed

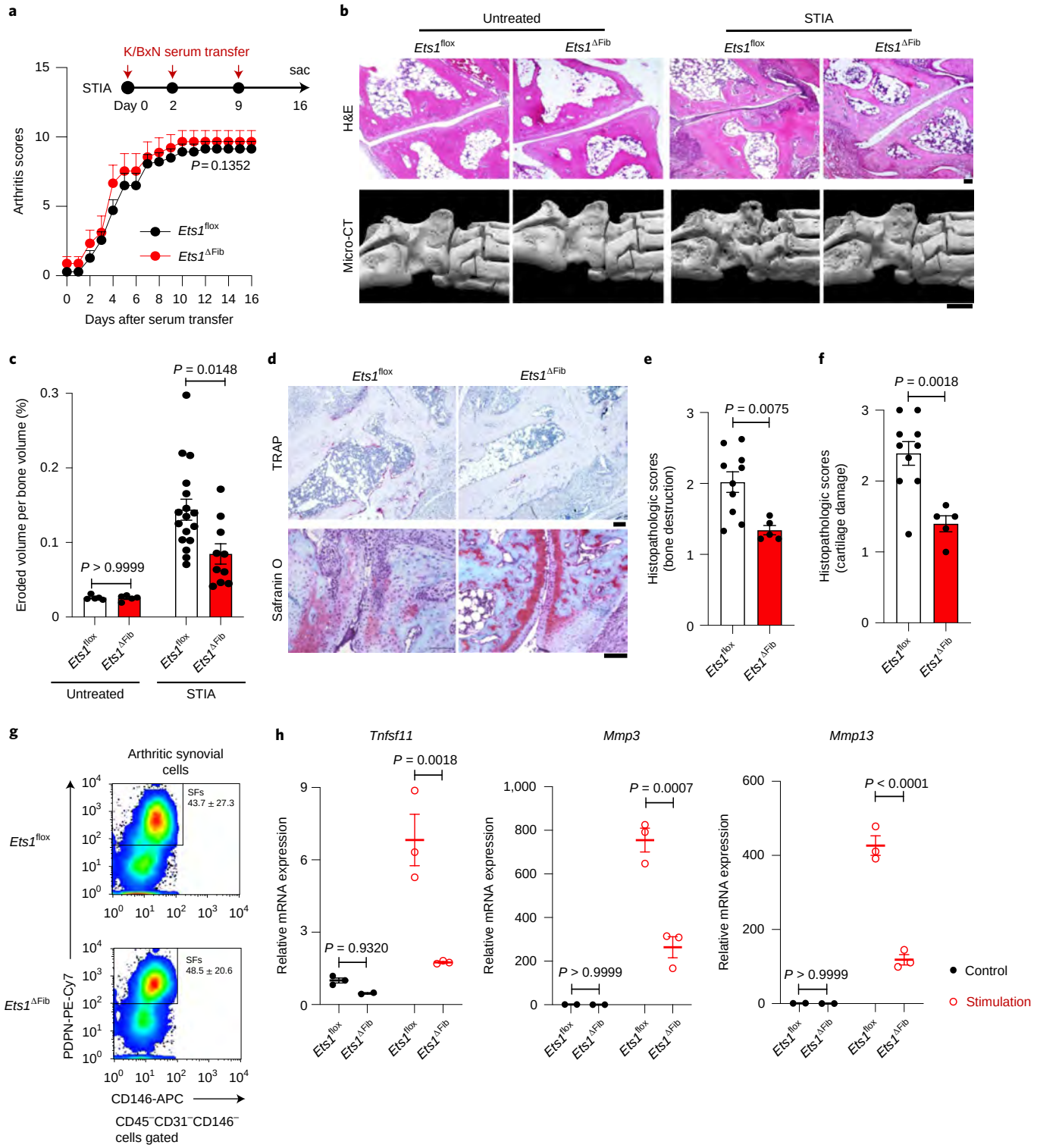

Fig. 4 | *Ets1* deletion in synovial fibroblasts attenuates arthritic joint damage. a, Arthritis scores of *Ets1*^{flox} mice (as control, $n=14$) and *Ets1*$^{\Delta Fib}$ mice ($n=9$) under persistent STIA condition[14]. Data are expressed as the mean ± s.e.m. *P* values were determined by two-tailed Mann–Whitney *U* test. **b**, Representative hematoxylin and eosin (H&E) and micro-CT images of ankle joints of *Ets1*^{flox} and *Ets1*$^{\Delta Fib}$ mice under untreated and STIA (day 16) conditions ($n=5$–10). Histology scale bar, 100 µm; micro-CT scale bar, 1 mm. **c**, Eroded volume per bone volume of the ankle joints of *Ets1*^{flox} mice (untreated, $n=5$; STIA, $n=17$) and *Ets1*$^{\Delta Fib}$ mice (untreated, $n=5$; STIA, $n=10$) analyzed by micro-CT. Data are expressed as the mean ± s.e.m. *P* values were determined by two-way ANOVA followed by Tukey's post hoc test. **d**, Representative TRAP and Safranin O staining images of the histological sections of ankle joints of *Ets1*^{flox} and *Ets1*$^{\Delta Fib}$ STIA (day 16) mice ($n=5$–10). Scale bars, 100 µm. **e**,**f**, Histopathologic scores for bone destruction (**e**) and cartilage damage (**f**) of *Ets1*^{flox} mice ($n=10$) and *Ets1*$^{\Delta Fib}$ mice ($n=5$). Data are expressed as the mean ± s.e.m. *P* values were determined by two-tailed *t*-test. **g**, Representative fluorescence-activated cell sorting (FACS) plot and gating strategies of SFs from STIA *Ets1*^{flox} mice ($n=12$) and *Ets1*$^{\Delta Fib}$ mice ($n=8$). Data are expressed as the mean ± s.e.m. **h**, mRNA expression levels of *Tnfsf11*, *Mmp3* and *Mmp13* in arthritic SFs that were isolated from *Ets1*^{flox} and *Ets1*$^{\Delta Fib}$ mice ($n=3$, 2 (*Ets1*^{flox}, *Ets1*$^{\Delta Fib}$) in *Tnfsf11* (control); $n=3$, 3 in *Tnfsf11* (stimulation); *Mmp3* and *Mmp13*, $n=2$, 2 in (control) and $n=3$, 3 in (stimulation)). Data are the mean ± s.e.m of independent biological samples. *P* values were determined by two-way ANOVA followed by Tukey's post hoc test.

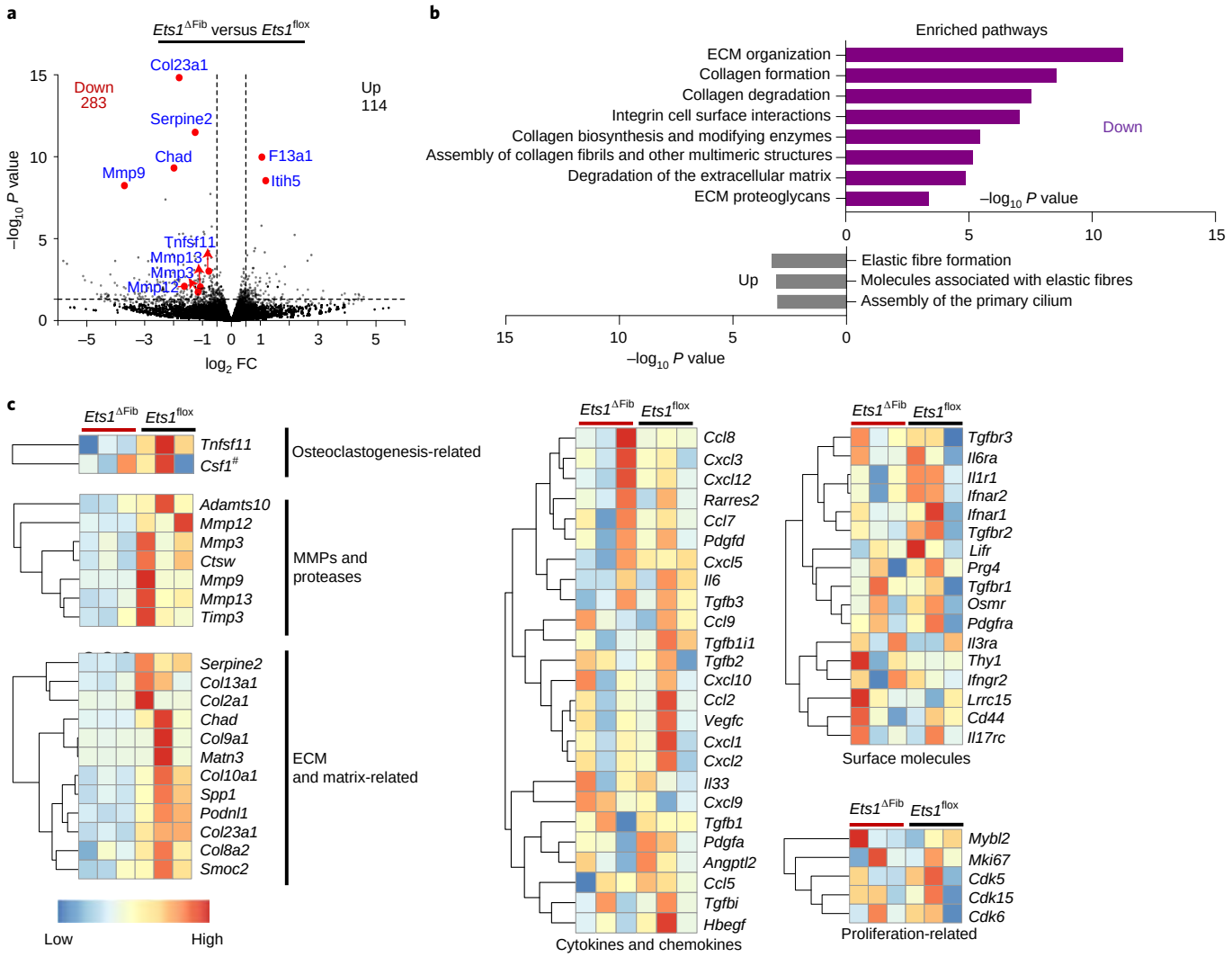

Fig. 5 | Transcriptome analysis of *Ets1*-deleted fibroblasts. a, Volcano plot showing the $\log_2$ fold change (FC) against $-\log_{10}$ *P* value comparing fibroblasts from *Ets1*^{flox} and *Ets1*$^{\Delta Fib}$ mice (STIA, $n=3$ per group) analyzed by DESeq2 (Wald test with Benjamini–Hochberg method correction). **b**, Pathway enrichment analysis on differentially expressed genes using the Reactome database with web-based tool BioJupies (Fisher's exact test). ECM, extracellular matrix. **c**, Heat maps showing the expression of representative differentially expressed genes in each sample (fibroblasts derived from *Ets1*^{flox} mice and *Ets1*$^{\Delta Fib}$ mice, $n=3$ per group; *Csf1* is annotated by a hash symbol and the genes in the categories 'cytokines and chemokines', 'surface molecules' and 'proliferation-related' were not significant as differentially expressed genes).

tomography (micro-CT) analysis indicated that arthritis-associated bone erosion was significantly reduced in the *Ets1*$^{\Delta Fib}$ mice (Fig. 4b,c). Histological analysis using tartrate-resistant acid phosphatase (TRAP) staining on the arthritic joint sections revealed abundant osteoclasts in *Ets1*^{flox} mice, whereas *Ets1*$^{\Delta Fib}$ mice exhibited a significant prevention of osteoclast formation and bone destruction (Fig. 4d,e). Safranin O staining suggested that *Ets1*$^{\Delta Fib}$ mice were also markedly protected from arthritis-associated cartilage damage (Fig. 4d,f).

Flow cytometry analysis indicated that the number and frequency of SFs were equivalent in the *Ets1*^{flox} and *Ets1*$^{\Delta Fib}$ mice (Fig. 4g and Extended Data Fig. 4g). We collected SFs from the *Ets1*^{flox} and *Ets1*$^{\Delta Fib}$ mice and found that *Ets1* deletion significantly decreased the expression levels of *Tnfsf11*, *Mmp3* and *Mmp13* in the arthritic SFs (Fig. 4h). A previous report showed that NOTCH3 signaling drives the expansion of inflammatory, but not tissue-destructive fibroblasts[33]. We analyzed the cell number of NOTCH3$^+$ inflammatory fibroblasts and ETS1$^+$ tissue-destructive fibroblasts during the inflammation and destruction phases in a CIA model (Extended Data Fig. 5a,b). The number of NOTCH3$^+$ fibroblasts was higher than the ETS1$^+$ fibroblast number in the inflammation phase, whereas there were more ETS1$^+$ fibroblasts in the destruction phase (Extended Data Fig. 5b). These data suggested that the change in fibroblast proportion is associated with the transition from the inflammation to destruction phase in arthritis.

Next, we performed bulk RNA-seq analyses on SFs isolated from arthritis-induced *Ets1*^{flox} and *Ets1*$^{\Delta Fib}$ mice (Extended Data Fig. 6a–c). A comprehensive gene expression analysis showed that *Ets1* deletion decreased the expression levels of 283 genes ($\log_2$ fold change < -0.5, $P < 0.05$) including *Mmp9*, *Tnfsf11*, *Mmp13*, *Mmp3* and *Mmp12* (Fig. 5a). Functional annotation of the *Ets1*-regulated genes showed a strong enrichment of the tissue-remodeling-related terms such as 'extracellular matrix organization', 'collagen formation' and 'collagen degradation' (Fig. 5b). The downregulated genes in *Ets1*-deleted fibroblasts also include proteases such as the one encoded by *Adamts10* and extracellular matrix-related genes such as *Col23a1* and *Spp1*. *Ets1* deletion did not influence the expression of cytokines, chemokines or cytokine receptors (such as those

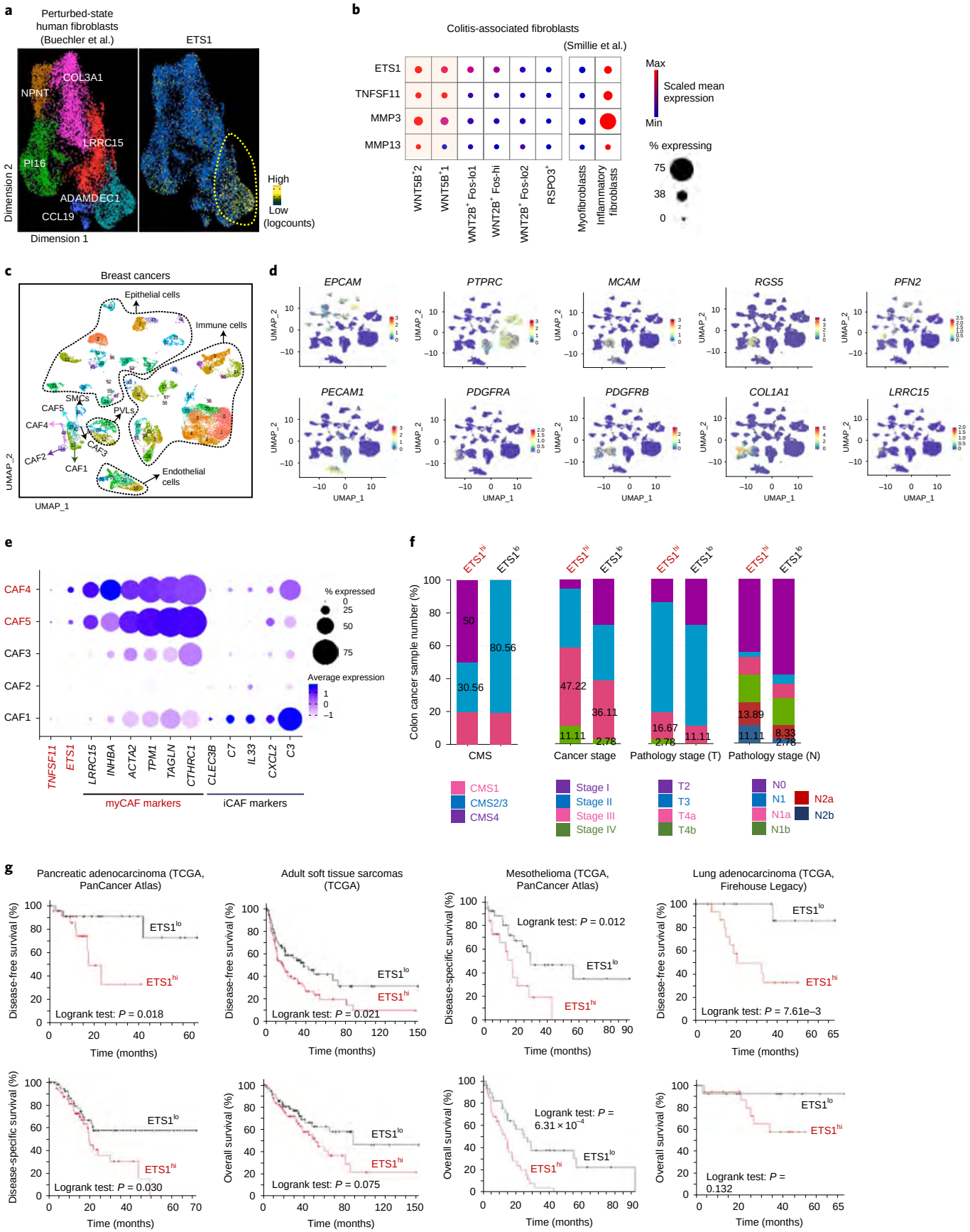
a
Perturbed-state human fibroblasts (Buechler et al.)
ETS1
COL3A1
NPNT
LRRC15
PI16
ADAMDEC1
CCL19
Dimension 2
Dimension 1
High
Low (logcounts)
b
Colitis-associated fibroblasts (Smillie et al.)
ETS1
TNFSF11
MMP3
MMP13
WNT5B+2
WNT5B+1
WNT2B+ Fos-lo1
WNT2B+ Fos-hi
WNT2B+ Fos-lo2
RSPO3+
Myofibroblasts
Inflammatory fibroblasts
Max
Scaled mean expression
Min
% expressing
75
38
0
c
Breast cancers
Epithelial cells
Immune cells
SMCs
PVLs
CAF5
CAF4
CAF3
CAF2
CAF1
Endothelial cells
UMAP_2
UMAP_1
d
EPCAM
PTPRC
MCAM
RGS5
PFN2
PECAM1
PDGFRA
PDGFRB
COL1A1
LRRC15
e
CAF4
CAF5
CAF3
CAF2
CAF1
% expressed
Average expression
TNFSF11
ETS1
LRRC15
INHBA
ACTA2
TPM1
TAGLN
CTHRC1
CLEC3B
C7
IL33
CXCL2
C3
myCAF markers
iCAF markers
f
ETS1hi
ETS1lo
Colon cancer sample number (%)
50
30.56
80.56
47.22
11.11
36.11
2.78
16.67
11.11
13.89
8.33
CMS
Cancer stage
Pathology stage (T)
Pathology stage (N)
CMS1
CMS2/3
CMS4
Stage I
Stage II
Stage III
Stage IV
T2
T3
T4a
T4b
N0
N1
N1a
N2a
N2b
g
Pancreatic adenocarcinoma (TCGA, PanCancer Atlas)
Adult soft tissue sarcomas (TCGA)
Mesothelioma (TCGA, PanCancer Atlas)
Lung adenocarcinoma (TCGA, Firehouse Legacy)
Disease-free survival (%)
Disease-specific survival (%)
Overall survival (%)
Time (months)
Logrank test: P = 0.018
Logrank test: P = 0.021
Logrank test: P = 0.012
Logrank test: P = 7.61e–3
Logrank test: P = 0.030
Logrank test: P = 0.075
Logrank test: P = 6.31 × 10−4
Logrank test: P = 0.132

Fig. 6 | Cross-tissue analysis of fibroblast single-cell datasets reveals the ETS1 expression is associated with perturbation-specific fibroblast phenotypes. a, Human perturbed-state fibroblasts atlas[4] (https://www.fibroxplorer.com/home) and the expression of ETS1 in the UMAP clusters colored by ETS1 logcounts. **b**, Dot plot showing the expression of ETS1, TNFSF11, MMP3 and MMP13 across the ulcerative colitis-associated fibroblast clusters[34]. **c**, UMAP visualization of human breast cancer cells[38] (GSE176078) colored by cluster ($n=100{,}064$ cells). SMCs, smooth muscle cells; PVLs, perivascular-like cells. **d**, Feature plot showing the expression of representative cell-type marker genes corresponding to the assigned cell types shown in **c**. **e**, Dot plot showing the expression of selected genes in the identified CAF clusters. **f**, CMS, cancer stage, pathology T stage and pathology N stage in individuals with colon cancer (Clinical Proteomic Tumor Analysis Consortium 2 (CPTAC-2), $n=110$)[58] divided by high or low levels of *ETS1* gene expression. The graphs show the individuals in the top third versus bottom third for the ETS1 expression (top third ETS1^{hi}, $n=36$; bottom third ETS1^{lo}, $n=36$). The number indicates the percentage of the indicated subtypes in each group. **g**, Kaplan–Meier survival plots comparing the individuals with pancreatic adenocarcinoma (TCGA, PanCancer Atlas, 184 samples, top third ETS1^{hi}, $n=60$; bottom third ETS1^{lo}, $n=62$), adult soft tissue sarcomas (TCGA, 206 samples, top third ETS1^{hi}, $n=70$; bottom third ETS1^{lo}, $n=72$), mesothelioma (TCGA, PanCancer Atlas, 87 samples, top third ETS1^{hi}, $n=29$; bottom third ETS1^{lo}, $n=29$) and lung adenocarcinoma (TCGA, Firehouse Legacy, 586 samples, samples with mRNA data ETS1^{hi}, $n=17$; ETS1^{lo}, $n=15$). *P* values were calculated by logrank test.

encoded by *Il6*, *Cxcl2* and *Osmr*; Fig. 5c), indicating that ETS1 is not involved in the inflammatory gene expression program in SFs.

Because there was no difference in the onset rate or disease severity between *Ets1*^{flox} and *Ets1*$^{\Delta Fib}$ mice, it is likely that ETS1 is required for the polarization toward the tissue-destructive activity but dispensable for the acquisition of the pro-inflammatory phenotype in SFs under arthritic conditions. Collectively, these findings demonstrate that ETS1 controls the transcription program of the joint-damaging factors RANKL and MMPs through distal enhancer regulation, thus serving as the key transcription factor driving pathogenic polarization of tissue-destructive fibroblasts in arthritis.

ETS1 expression in pathogenic fibroblasts across diseases. A recent study integrating scRNA-seq datasets across 17 tissues, 12 diseases and 2 species identified perturbation-specific activated fibroblast states that are not observed in the steady state[4]. Using the single-cell fibroblast atlases, we found that ETS1 is highly expressed in ADAMDEC1^{+} colitis-associated fibroblasts as well as in LRRC15^{+} cancer-associated fibroblasts (CAFs) in both human and mouse (Fig. 6a and Extended Data Fig. 7a,b).

To further examine the expression pattern of ETS1 in colitis-associated and cancer-associated fibroblasts, we analyzed the scRNA-seq datasets derived from individuals with ulcerative colitis[34] and those with colorectal cancer[35] (Single Cell Portal SCP259 and GSE178341). We found that the ETS1 expression levels in ulcerative colitis-associated and colorectal cancer-associated stromal cells were much higher than in healthy controls (Extended Data Fig. 7c,d). Sub-clustering analysis of fibroblast populations of individuals with ulcerative colitis showed that ETS1 is highly expressed in WNT5B^{+} crypt-top fibroblasts[36,37] but not WNT2B^{+} and RSPO3^{+} crypt-bottom fibroblasts[36,37] (Fig. 6b), suggesting the properties of ETS1-expressing fibroblasts in colitis, analogous to RA, may also be shaped by their distinct anatomical location. In fibroblast populations of individuals with colorectal cancer, the ETS1 expression is strongly enriched in CAF clusters: MMP3^{+} CAFs, GREM1^{+} CAFs and CXCL14^{+} CAFs (Extended Data Fig. 7e).

In various cancers, CAFs are segregated into two major subtypes: the matrix remodeling myofibroblastic CAFs and immune-interacting inflammatory CAFs[38–40]. We analyzed a scRNA-seq dataset of human breast cancers (GSE176078)[38] and found that *ETS1* and *TNFSF11* are specifically expressed in myofibroblastic CAF populations (CAF4 and CAF5, characterized by high expression levels of *LRRC15*, *INHBA*, *ACTA2*, *TPM1*, *TAGLN* and *CTHRC1*), but not in the inflammatory CAFs cluster (CAF1, characterized by expression of *CXCL2*, *C3*, *IL33*, *C7* and *CLEC3B*; Fig. 6c–e). Because CAF plays a critical pathological role in cancer progression, we tested the correlation between the expression of ETS1 in cancer lesions and the pathological outcomes of individuals with cancer. Using the The Cancer Genome Atlas (TCGA) datasets of individuals with colorectal cancer, we found that a high ETS1 expression was strongly enriched in consensus molecular subtype 4 (CMS4) tumors (Fig. 6f), a tumor subtype that is characterized by prominent mesenchymal activation and stromal invasion with a worse prognosis compared to the other subtypes (CMS1–3)[41]. In concordance, ETS1^{hi} tumors are highly associated with more advanced cancer (stages III and IV) and pathology (tumor (T) stages T4a and T4b, and node (N) stages N2a and N2b; Fig. 6f). In pancreatic adenocarcinoma, adult soft tissue sarcomas, mesothelioma and lung adenocarcinoma, we also found that a high ETS1 expression was significantly associated with a poor prognosis in these individuals with cancer (Fig. 6g). As in the arthritic SFs, the expression level of ETS1 positively correlated with that of RANKL and MMPs in the cancer-associated and colitis-associated fibroblasts (Fig. 6b and Extended Data Fig. 7a–f). Although the role of fibroblast RANKL in such diseases has yet to be addressed, ETS1-mediated MMP production by activated fibroblasts may contribute to tissue remodeling in various disease settings. Intriguingly, we found that genetic variants of *ETS1* are commonly associated with multiple diseases including

Fig. 7 | *Ets1*-expressing fibroblasts contribute to tissue remodeling and healing upon epithelial injury. a, UMAP embedding of 24,566 colon fibroblasts (GSE172261)[43] derived from DSS-fed mice colored by cluster. Annotation of the fibroblast subtypes is based on the expression of known marker genes[43] (Fig. 7b). **b**, Dot plot showing the expression of selected genes in the identified fibroblast clusters. **c**, Representative immunofluorescence images of colons from DSS-fed mice ($n=3$). **d**, Body weight loss in *Ets1*^{flox} mice ($n=10$) and *Ets1*$^{\Delta Fib}$ mice ($n=11$) administered with 2.5% DSS for 7 d and normal drinking water for 3 d. Untreated mice received normal drinking water throughout the experiments (*Ets1*^{flox} mice, $n=6$; *Ets1*$^{\Delta Fib}$ mice, $n=7$). *P* values were determined by two-tailed Mann–Whitney *U* test. **e**,**f**, Representative images of colons (**e**) and quantification of the colon length (**f**) from untreated mice (*Ets1*^{flox} mice, $n=6$; *Ets1*$^{\Delta Fib}$ mice, $n=7$) and DSS-fed mice (*Ets1*^{flox} mice, $n=7$; *Ets1*$^{\Delta Fib}$ mice, $n=10$) at day 10. *P* values were determined by two-way ANOVA analysis followed by Sidak's multiple-comparisons test. **g**,**h**, Quantification of the disease activity index[59] at the indicated time point (day 7, *Ets1*^{flox} mice $n=10$ and *Ets1*$^{\Delta Fib}$ mice $n=11$; day 10, *Ets1*^{flox} mice $n=7$ and *Ets1*$^{\Delta Fib}$ mice $n=8$; **g**) and spleen weight per body weight at day 10 in untreated mice (*Ets1*^{flox}, $n=6$; *Ets1*$^{\Delta Fib}$, $n=7$) and DSS-fed mice (*Ets1*^{flox}, $n=7$; *Ets1*$^{\Delta Fib}$, $n=8$; **h**). *P* values were determined by two-way ANOVA analysis followed by Sidak's multiple-comparisons test. **i**, Representative H&E and trichrome staining images of colons from *Ets1*^{flox} and *Ets1*$^{\Delta Fib}$ mice at day 10 after DSS administration, $n=6$–8. **j**,**k**, Thickness of submucosa (**j**) and muscularis propria (**k**) of the stained colon sections prepared from untreated mice (*Ets1*^{flox}, $n=6$; *Ets1*$^{\Delta Fib}$, $n=7$) and DSS-fed mice (*Ets1*^{flox}, $n=7$; *Ets1*$^{\Delta Fib}$, $n=8$). Data are shown as the mean ± s.e.m. *P* values were determined by two-way ANOVA analysis followed by Sidak's multiple-comparisons test. Scale bars, 100 μm.

inflammatory bowel diseases, psoriasis, primary sclerosing cholangitis, ankylosing spondylitis, RA and systemic lupus erythematosus[27,30,42]. Collectively, these findings suggest that the dysregulation of ETS1 expression may represent a shared mechanism regulating the pathogenic fibroblast phenotypes in various diseases.

ETS1⁺ fibroblasts contribute to tissue remodeling in colitis. To test the role of ETS1-expressing fibroblasts in other diseases, we utilized the dextran sulfate sodium (DSS)-induced colitis model, which is widely used to study the pathogenesis of inflammatory bowel diseases[43]. The scRNA-seq data (GSE172261)[43] of mesenchymal cells collected from the DSS-induced colitis lesions showed that ETS1 is exclusively expressed in the crypt-top fibroblasts (known to express bone morphogenetic proteins and noncanonical Wnt ligands and contribute to epithelial differentiation and remodeling[36,37,43,44]), but not in the crypt-bottom inflammation-associated fibroblasts that express *Il6*, *Thy1* and *Grem1* (refs. [3,34,43]; Fig. 7a,b and Extended Data Fig. 8a,b). Immunohistochemistry confirmed that the ETS1-expressing fibroblasts in the intestine were mainly located at the top of the colonic crypt (Fig. 7c), indicating that ETS1 is highly expressed by the tissue-remodeling fibroblast subset in colitis.

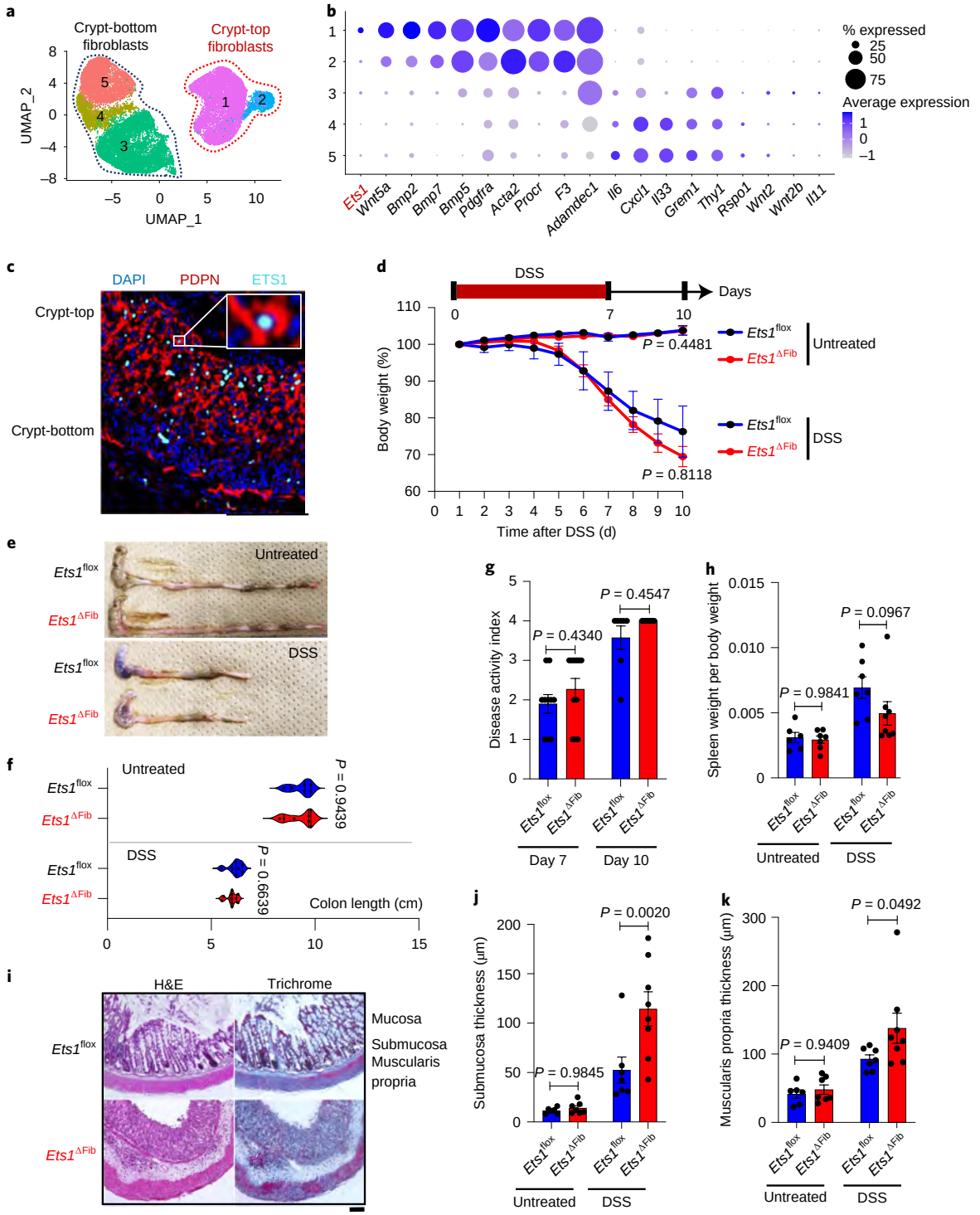

Although *Col6a1*-Cre targets only SFs in the skeletal system, it was reported that this Cre recombinase is expressed in the intestinal fibroblasts[31,45]. To test the role of ETS1-expressing fibroblasts in vivo, we induced a DSS-induced colitis model into the *Ets1*^{flox} and *Ets1*$^{\Delta Fib}$ mice. ETS1 deletion did not affect intestinal homeostasis at steady state (Fig. 7d–f). Under the DSS-induced colitis conditions, there was no significant difference in colon length, spleen weight and disease activity index (assessed by standard parameters including the body weight loss, stool consistency and the presence of diarrhea and bleeding) between the *Ets1*^{flox} and *Ets1*$^{\Delta Fib}$ mice, suggesting that ETS1 deletion did not affect the inflammation level (Fig. 7d–h). However, the *Ets1*$^{\Delta Fib}$ mice displayed a defect in mucosal remodeling and healing accompanied with an aberrant matrix accumulation in the submucosa and muscularis propria areas (Fig. 7i–k and Extended Data Fig. 8c). Thus, ETS1-expressing fibroblasts are involved in tissue remodeling and epithelial healing but not in inflammation during colitis.

Intriguingly, the ETS1-expressing fibroblasts are preferentially localized to the hypoxic regions in both arthritis and colitis (the top of the colonic crypt[46] and the lining layer of the synovium in the joint[47]). Chromatin analysis of the *ETS1* gene locus by Hi-C sequencing, ChIP–seq and ATAC–seq suggested that ETS1 expression is regulated by hypoxia-inducible factors (HIFs) in fibroblasts (Extended Data Fig. 9a–c). Histological analyses showed the HIF2 expression in the synovial lining fibroblasts and intestinal crypt-top fibroblasts, which highly express ETS1 (Extended Data Fig. 9d). There was a positive correlation between ETS1 and HIF2 expression levels in fibroblasts in arthritis and inflammatory bowel diseases (Extended Data Fig. 9e). Thus, in addition to the inflammatory cytokines, hypoxia may function as a local cue contributing to the ETS1 expression in fibroblasts.

A previous report showed that PU.1 drives the polarization toward matrix-producing pro-fibrotic fibroblasts and contributes to the pathogenesis of fibrotic diseases[48]. To gain insights into the relationship between ETS1-expressing and PU.1-expressing fibroblasts, we analyzed the scRNA-seq datasets from various fibrosis tissues, including the liver (GSE136103)[49], lung (GSE135893)[50] and kidney (GSE140023)[51], and found that the expression of ETS1 and PU.1 (encoded by *SPI1*) in fibroblasts in fibrotic lesions is almost mutually exclusive (Extended Data Fig. 10a–o). Immunohistochemistry on the pulmonary fibrosis lesions and the arthritic synovium confirmed that the expression of PU.1 and ETS1 was not overlapped in fibroblasts (Extended Data Fig. 10p,q). A previous report showed that hepatic stellate cell-specific deletion of *Ets1* exacerbated fibrosis in a carbon tetrachloride-induced liver fibrosis model[52]. Because ETS1 promotes the expression of MMPs and MMP-mediated matrix degradation was reported to contribute to the resolution of fibrosis[53], we suspect that the ETS1-expressing fibroblasts may function as a double-edged sword inducing tissue damage while also contributing to fibrosis resolution.

In summary, our data suggest that ETS1 may function as a key transcription factor regulating the tissue-remodeling fibroblast phenotypes in various diseases.

Discussion

The destruction of bone and cartilage results in a loss of joint functionality, critically impairing the quality of life in individuals with arthritis. Accumulating evidence has demonstrated that RANKL and osteoclasts are the central players in arthritis-induced bone damage[10], and the anti-RANKL antibody denosumab was shown to inhibit the progression of bone erosion in individuals with RA in randomized controlled studies[54,55]. However, denosumab does not reduce cartilage destruction[54,55]. To date, there is no therapeutic option that specifically and directly prevents both bone and cartilage damage in individuals with RA. In this study, we demonstrated that fibroblast-specific deletion of ETS1 efficiently attenuates arthritis-induced structural damage by inhibiting both bone and cartilage destruction, suggesting that the targeting of tissue-destructive fibroblasts is a promising and conceptually new strategy for the treatment of joint damage in individuals with RA.

Although a diverse array of functional fibroblast subsets has been described in the current studies[2,3,5,6,38,39,43,56], the perturbation-specific activated fibroblast states can be divided into two main phenotypes: pro-inflammatory (or immune-interacting) and tissue-destructive (or tissue-remodeling)[3–6]. We identified ETS1 as a key transcription factor driving polarization of tissue-destructive fibroblasts in RA and found that ETS1 expression is also associated with pathogenic fibroblast phenotypes in multiple diseases including colitis and cancer. While ETS1-expressing fibroblasts play a fundamental role in tissue destruction in arthritis, they are involved in mucosal tissue remodeling and healing in colitis. Thus, it is likely that ETS1-expressing fibroblasts play a universal role in tissue remodeling but contribute to each disease pathogenesis specifically in a context-dependent manner.

ETS1 is a member of the ETS-domain transcription factors, a well-conserved transcription factor family found in all metazoan organisms[25]. The importance of ETS transcription factors has been well documented in hematopoiesis, in which ETS1 regulates lymphopoiesis while PU.1 controls myelopoiesis[26]. Given that ETS1 drives the polarization toward matrix-degrading tissue-remodeling fibroblasts in arthritis, whereas PU.1 regulates the matrix-producing tissue-remodeling fibroblasts in fibrosis, the ETS transcription factors are evidently critically involved in the regulation of a variety of 'tissue-remodeling' fibroblast phenotypes under pathological conditions, the mechanisms underlying which will be a critically important subject to pursue in future work. Further studies are required to clarify the pathological relevance of ETS transcription factors expressed in fibroblasts in various disease settings.

Single-cell technology has brought about a new era in life science in which cellular heterogeneity is investigated at an unprecedented level of resolution and the biological systems are described by the data gathered from individual cells. As ETS1 drives the pathological tissue-remodeling programs in disease-associated fibroblasts, various fibroblast functions across biological contexts may also be controlled by certain shared transcriptomic and epigenetic mechanisms. Structural cells such as fibroblasts have recently attracted considerable attention as choreographers of the tissue homeostasis[56]. Investigation into the molecular mechanisms underlying fibroblast functions will be a key to understanding human physiology and diseases.

Online content

Any methods, additional references, Nature Research reporting summaries, source data, extended data, supplementary information, acknowledgements, peer review information; details of author contributions and competing interests; and statements of data and code availability are available at https://doi.org/10.1038/s41590-022-01285-0.

Received: 10 December 2021; Accepted: 8 July 2022;
Published online: 23 August 2022

References

1. Virchow, R. *Die cellularpathologie in ihrer begründung auf physiologische und pathologische gewebelehre. Zwanzig vorlesungen gehalten während der monate februar, märz und april 1858 im Pathologischen institute zu Berlin* (A. Hirschwald, 1858).
2. Plikus, M. V. et al. Fibroblasts: origins, definitions, and functions in health and disease. *Cell* **184**, 3852–3872 (2021).
3. Davidson, S. et al. Fibroblasts as immune regulators in infection, inflammation and cancer. *Nat. Rev. Immunol.* https://doi.org/10.1038/s41577-021-00540-z (2021).
4. Buechler, M. B. et al. Cross-tissue organization of the fibroblast lineage. *Nature* **593**, 575–579 (2021).

5. Koliaraki, V., Prados, A., Armaka, M. & Kollias, G. The mesenchymal context in inflammation, immunity and cancer. *Nat. Immunol.* **21**, 974–982 (2020).
6. Buckley, C. D. Fibroblast cells reveal their ancestry. *Nature* **593**, 511–512 (2021).
7. Buckley, C. D. et al. Immune-mediated inflammation across disease boundaries: breaking down research silos. *Nat. Immunol.* **22**, 1344–1348 (2021).
8. Danks, L. et al. RANKL expressed on synovial fibroblasts is primarily responsible for bone erosions during joint inflammation. *Ann. Rheum. Dis.* **75**, 1187–1195 (2016).
9. Komatsu, N. et al. Plasma cells promote osteoclastogenesis and periarticular bone loss in autoimmune arthritis. *J. Clin. Invest.* https://doi.org/10.1172/JCI143060 (2021).
10. Tsukasaki, M. & Takayanagi, H. Osteoimmunology: evolving concepts in bone–immune interactions in health and disease. *Nat. Rev. Immunol.* **19**, 626–642 (2019).
11. Takayanagi, H. et al. T cell-mediated regulation of osteoclastogenesis by signalling cross-talk between RANKL and IFN-γ. *Nature* **408**, 600–605 (2000).
12. Takayanagi, H. et al. Involvement of receptor activator of nuclear factor κB ligand/osteoclast differentiation factor in osteoclastogenesis from synoviocytes in rheumatoid arthritis. *Arthritis Rheum.* **43**, 259–269 (2000).
13. Takayanagi, H. et al. A new mechanism of bone destruction in rheumatoid arthritis: synovial fibroblasts induce osteoclastogenesis. *Biochem. Biophys. Res. Commun.* **240**, 279–286 (1997).
14. Croft, A. P. et al. Distinct fibroblast subsets drive inflammation and damage in arthritis. *Nature* **570**, 246–251 (2019).
15. Stephenson, W. et al. Single-cell RNA-seq of rheumatoid arthritis synovial tissue using low-cost microfluidic instrumentation. *Nat. Commun.* **9**, 791 (2018).
16. Zhang, F. et al. Defining inflammatory cell states in rheumatoid arthritis joint synovial tissues by integrating single-cell transcriptomics and mass cytometry. *Nat. Immunol.* **20**, 928–942 (2019).
17. Bishop, K. A. et al. Transcriptional regulation of the human *TNFSF11* gene in T cells via a cell type-selective set of distal enhancers. *J. Cell. Biochem.* **116**, 320–330 (2015).
18. Onal, M. et al. Unique distal enhancers linked to the mouse *Tnfsf11* gene direct tissue-specific and inflammation-induced expression of RANKL. *Endocrinology* **157**, 482–496 (2016).
19. Loh, C. et al. TNF-induced inflammatory genes escape repression in fibroblast-like synoviocytes: transcriptomic and epigenomic analysis. *Ann. Rheum. Dis.* **78**, 1205–1214 (2019).
20. Krishna, V. et al. Integration of the transcriptome and genome-wide landscape of BRD2 and BRD4 binding motifs identifies key superenhancer genes and reveals the mechanism of Bet inhibitor action in rheumatoid arthritis synovial fibroblasts. *J. Immunol.* **206**, 422–431 (2021).
21. Andersson, R. & Sandelin, A. Determinants of enhancer and promoter activities of regulatory elements. *Nat. Rev. Genet.* **21**, 71–87 (2020).
22. Kollias, G. et al. Animal models for arthritis: innovative tools for prevention and treatment. *Ann. Rheum. Dis.* **70**, 1357–1362 (2011).
23. Alves, C. H., Farrell, E., Vis, M., Colin, E. M. & Lubberts, E. Animal models of bone loss in inflammatory arthritis: from cytokines in the bench to novel treatments for bone loss in the bedside—a comprehensive review. *Clin. Rev. Allergy Immunol.* **51**, 27–47 (2016).
24. Tsuchiya, H. et al. Parsing multiomics landscape of activated synovial fibroblasts highlights drug targets linked to genetic risk of rheumatoid arthritis. *Ann. Rheum. Dis.* https://doi.org/10.1136/annrheumdis-2020-218189 (2020).
25. Bartel, F. O., Higuchi, T. & Spyropoulos, D. D. Mouse models in the study of the Ets family of transcription factors. *Oncogene* **19**, 6443–6454 (2000).
26. Laslo, P. et al. Multilineage transcriptional priming and determination of alternate hematopoietic cell fates. *Cell* **126**, 755–766 (2006).
27. Okada, Y. et al. Genetics of rheumatoid arthritis contributes to biology and drug discovery. *Nature* **506**, 376–381 (2014).
28. Nakamura, Y. et al. Ets-1 regulates TNF-α-induced matrix metalloproteinase-9 and tenascin expression in primary bronchial fibroblasts. *J. Immunol.* **172**, 1945–1952 (2004).
29. Redlich, K. et al. Overexpression of transcription factor Ets-1 in rheumatoid arthritis synovial membrane: regulation of expression and activation by interleukin-1 and tumor necrosis factor alpha. *Arthritis Rheum.* **44**, 266–274 (2001).
30. Kim, C. J. et al. The transcription factor Ets1 suppresses T follicular helper type 2 cell differentiation to halt the onset of systemic lupus erythematosus. *Immunity* **50**, 272 (2019).
31. Armaka, M. et al. Mesenchymal cell targeting by TNF as a common pathogenic principle in chronic inflammatory joint and intestinal diseases. *J. Exp. Med.* **205**, 331–337 (2008).
32. Culemann, S. et al. Locally renewing resident synovial macrophages provide a protective barrier for the joint. *Nature* **572**, 670–675 (2019).
33. Wei, K. et al. Notch signalling drives synovial fibroblast identity and arthritis pathology. *Nature* **582**, 259–264 (2020).
34. Smillie, C. S. et al. Intra- and inter-cellular rewiring of the human colon during ulcerative colitis. *Cell* **178**, 714–730 (2019).
35. Pelka, K. et al. Spatially organized multicellular immune hubs in human colorectal cancer. *Cell* **184**, 4734–4752 (2021).
36. Brügger, M. D., Valenta, T., Fazilaty, H., Hausmann, G. & Basler, K. Distinct populations of crypt-associated fibroblasts act as signaling hubs to control colon homeostasis. *PLoS Biol.* **18**, e3001032 (2020).
37. Karpus, O. N. et al. Colonic CD90$^+$ crypt fibroblasts secrete semaphorins to support epithelial growth. *Cell Rep.* **26**, 3698–3708 (2019).
38. Wu, S. Z. et al. A single-cell and spatially resolved atlas of human breast cancers. *Nat. Genet.* **53**, 1334–1347 (2021).
39. Öhlund, D. et al. Distinct populations of inflammatory fibroblasts and myofibroblasts in pancreatic cancer. *J. Exp. Med.* **214**, 579–596 (2017).
40. Dominguez, C. X. et al. Single-cell RNA sequencing reveals stromal evolution into LRRC15$^+$ myofibroblasts as a determinant of patient response to cancer immunotherapy. *Cancer Discov.* **10**, 232–253 (2020).
41. Guinney, J. et al. The consensus molecular subtypes of colorectal cancer. *Nat. Med.* **21**, 1350–1356 (2015).
42. Ellinghaus, D. et al. Analysis of five chronic inflammatory diseases identifies 27 new associations and highlights disease-specific patterns at shared loci. *Nat. Genet.* **48**, 510–518 (2016).
43. Jasso, G. J. et al. Colon stroma mediates an inflammation-driven fibroblastic response controlling matrix remodeling and healing. *PLoS Biol.* **20**, e3001532 (2022).
44. Kinchen, J. et al. Structural remodeling of the human colonic mesenchyme in inflammatory bowel disease. *Cell* **175**, 372–386 (2018).
45. Nagashima, K. et al. Targeted deletion of RANKL in M cell inducer cells by the *Col6a1*-Cre driver. *Biochem. Biophys. Res. Commun.* **493**, 437–443 (2017).
46. Singhal, R. & Shah, Y. M. Oxygen battle in the gut: hypoxia and hypoxia-inducible factors in metabolic and inflammatory responses in the intestine. *J. Biol. Chem.* **295**, 10493–10505 (2020).
47. Ryu, J. H. et al. Hypoxia-inducible factor-2α is an essential catabolic regulator of inflammatory rheumatoid arthritis. *PLoS Biol.* **12**, e1001881 (2014).
48. Wohlfahrt, T. et al. PU.1 controls fibroblast polarization and tissue fibrosis. *Nature* **566**, 344–349 (2019).
49. Ramachandran, P. et al. Resolving the fibrotic niche of human liver cirrhosis at single-cell level. *Nature* **575**, 512–518 (2019).
50. Habermann, A. C. et al. Single-cell RNA sequencing reveals profibrotic roles of distinct epithelial and mesenchymal lineages in pulmonary fibrosis. *Sci. Adv.* **6**, eaba1972 (2020).
51. Conway, B. R. et al. Kidney single-cell atlas reveals myeloid heterogeneity in progression and regression of kidney disease. *J. Am. Soc. Nephrol.* **31**, 2833–2854 (2020).
52. Liu, X. et al. Identification of lineage-specific transcription factors that prevent activation of hepatic stellate cells and promote fibrosis resolution. *Gastroenterology* **158**, 1728–1744 (2020).
53. Cabrera, S. et al. Delayed resolution of bleomycin-induced pulmonary fibrosis in absence of MMP13 (collagenase 3). *Am. J. Physiol. Lung Cell. Mol. Physiol.* **316**, L961–L976 (2019).
54. Cohen, S. B. et al. Denosumab treatment effects on structural damage, bone mineral density, and bone turnover in rheumatoid arthritis: a twelve-month, multicenter, randomized, double-blind, placebo-controlled, phase II clinical trial. *Arthritis Rheum.* **58**, 1299–1309 (2008).
55. Takeuchi, T. et al. Effect of denosumab on Japanese patients with rheumatoid arthritis: a dose-response study of AMG 162 (denosumab) in patients with rheumatoId arthritis on methotrexate to validate inhibitory effect on bone Erosion (DRIVE)—a 12-month, multicentre, randomised, double-blind, placebo-controlled, phase II clinical trial. *Ann. Rheum. Dis.* **75**, 983–990 (2016).
56. Krausgruber, T. et al. Structural cells are key regulators of organ-specific immune responses. *Nature* **583**, 296–302 (2020).
57. Kitazawa, R., Mori, K., Yamaguchi, A., Kondo, T. & Kitazawa, S. Modulation of mouse RANKL gene expression by Runx2 and vitamin D_3. *J. Cell. Biochem.* **105**, 1289–1297 (2008).
58. Vasaikar, S. et al. Proteogenomic analysis of human colon cancer reveals new therapeutic opportunities. *Cell* **177**, 1035–1049 (2019).
59. Khafipour, A. et al. Denosumab regulates gut microbiota composition and cytokines in dinitrobenzene sulfonic acid (DNBS)-experimental colitis. *Front. Microbiol.* **11**, 1405 (2020).

Methods

Human participant research. Human synovial tissue specimens were obtained from participants undergoing knee joint replacement surgery at The University of Tokyo Hospital. All the participants with RA ($n=4$, aged 69–77 years old, female $n=1$ and male $n=3$) fulfilled the 2010 American College of Rheumatology-European League Against Rheumatism criteria for the classification of RA and provided written informed consent. This study was approved by the Institutional Review Board at The University of Tokyo.

Mice. All mice were maintained under specific pathogen-free conditions, and all experiments were performed with the approval of the Institutional Review Board at The University of Tokyo. The animals were maintained at a constant ambient temperature of 22–26 degree, 40–65% of humidity under a 12-h light/dark cycle. No statistical methods were used to predetermine sample sizes, but our sample sizes were similar to those reported in previous publications[14,33]. All mice experiments were randomized and both male mice and female mice were used unless otherwise noted. No data or samples were excluded from the analyses. The individual data points are shown in the figures. Data distribution was assumed to be normal, but this was not formally tested.

C57BL/6J (B6) mice and DBA/1J mice were purchased from CLEA Japan and Charles River Laboratories Japan, respectively. *Col6a1*-Cre mice and *Ets1*^{flox} mice were previously described[30,31]. Fibroblast-specific *Ets1*-deficient mice (*Ets1*$^{\Delta Fib}$) were generated by breeding *Ets1*^{flox} mice with *Col6a1*-Cre mice. We used 8- to 12-week-old mice for all the experiments. Enhancer-KO mice (*E1*-KO, *E2*-KO and *E3*-KO) were generated by CRISPR–Cas9-mediated genome editing technology on the B6 background. Single-guide (sg) RNA and Cas9 mRNA were prepared as described previously. Sequences of sgRNAs, single-stranded oligonucleotides (ssODNs) and the primers for the detection of the deletion regions are shown in Supplementary Table 1. Individual enhancer deletion (*E1*, 2.8 kb; *E2*, 3.4 kb; *E3*, 1.2 kb) was confirmed by sequencing.

Arthritis induction. STIA was induced by intraperitoneal injection of 150 µl pooled serum collected from arthritic K/BxN mice (9 weeks) on day 0 and day 2 (analyzed on day 10 for enhancer-KO mice (B6 background)) or on day 0, day 2 and day 9 (analyzed on day 16 for *Ets1*^{flox} and *Ets1*$^{\Delta Fib}$ mice (B6 background)), as indicated. All experiments were performed on 8- to 12-week-old mice of both male and female mice. Randomization was used whenever possible to determine the experimental order. The animal numbers used in each experiment are described in the corresponding figure legends. Joint swelling was scored ranging from 0 to 3 per paw, with a maximal score of 12 per mouse. We judged the development of arthritis in the joints using the following criteria: 0, no joint swelling; 1, swelling of one paw joint; 2, mild swelling of the wrist or ankle; 3, severe swelling of the wrist or ankle. Data collection was not performed blind to the genotypes the animals.

AIA was induced on the enhancer-KO mice (8- to 12-week-old male and female mice). Briefly, mice were first systemically immunized with 200 µg methylated bovine serum album (mBSA; Sigma-Aldrich, A1009-250MG) dissolved in complete Freund's adjuvant (Difco Laboratories, 263810) containing heat-killed *Mycobacterium tuberculosis* H37Ra (BD Difco, 231141; 5 mg ml^{-1}) delivered intradermally. On day 7, the mice received a second immunization with 300 µg mBSA dissolved in 30 µl PBS delivered intraarticularly into the knee joint. Mice were injected with the same volume of PBS in the other side of the knee joint as a control. On day 14, mice were euthanized and analyzed as indicated.

For CIA, male DBA/1J mice were first immunized with an emulsion containing 50 µl of chicken type II collagen (Sigma-Aldrich, C9301, 4 mg ml^{-1}) and 50 µl incomplete Freund's adjuvant (Difco Laboratories, 263910) containing heat-killed *Mycobacterium tuberculosis* H37Ra (3.3 mg ml^{-1}) delivered intradermally at the base of the tail. On day 21, mice were re-challenged with the same emulsion as used in the primary immunization. The mice were then clinically assessed three times per week based on the criteria described above. In this experiment setting, days 28–42 after immunization was considered as the inflammation phase and day 42 onward was considered as the destruction phase based on our previous studies[8,9].

Dextran sulfate sodium-induced colitis. DSS-induced colitis was induced on the *Ets1*^{flox} and *Ets1*$^{\Delta Fib}$ mice (8- to 12-week-old male and female mice) by administration of 2.5% DSS (36–50 kDa; MP Biomedicals, 160110) in the drinking water for 7 d followed by 3 d of normal drinking water. Untreated mice received normal drinking water throughout the experiment. The disease activity index was evaluated daily on the standard parameters including body weight loss, stool consistency and the presence of diarrhea and bleeding, as previously reported[59]. Data collection was not performed blind to the genotypes of the animals. All mice were euthanized at day 10. Distal colons were isolated and subjected to 4% paraformaldehyde overnight for fixation, followed by 70% ethanol for another 24 h and then embedded into paraffin and sectioned (5 µm) for H&E and trichrome staining using Trichrome Stain Kit (Modified Gomori's, ScyTek, TRG-1) according to the manufacturer's instructions. The thickness of submucosa and muscularis propria area was evaluated using a BZ-II Analyzer (Keyence). For immunofluorescence staining, the frozen tissue blocks were cut into 8-µm-thick serial sections using a Cryostat (Leica), air-dried and stained with Rabbit ETS1 mAb (CST, D8O8A), Rabbit HIF2 Antibody (Novus Bio, NB100-122), anti-mouse Podoplanin Antibody (BioLegend, 8.1.1), anti-mouse Ep-CAM Antibody (BioLegend, G8.8), anti-Rabbit IgG secondary antibody (Invitrogen, A-31573), anti-Syrian hamster IgG secondary antibody (107-606-142, Jackson ImmunoResearch), anti-Rat IgG secondary antibody (Invitrogen, A-21209) and DAPI (Molecular Probes). The antibody dilution factor is described in the Nature Research Reporting Summary. Multicolor images were obtained with a Nikon C2 confocal microscope.

Pulmonary fibrosis model. We induced a pulmonary fibrosis model as previously described[60]. Briefly, 8- to 10-week-old male and female mice were anesthetized and intratracheally instilled with PBS and bleomycin (3 µg (2.88 units) per gram of body weight; Nippon Kayaku, 874234). The lungs were collected at day 14, fixed in 4% paraformaldehyde overnight and embedded in paraffin. Sections of 4 µm in thickness were stained with H&E and azan to identify the fibrotic lesions. Immunofluorescence staining was performed on the serial sections using the following antibodies: anti-mouse Podoplanin Antibody (BioLegend, 8.1.1), Rabbit ETS1 mAb (CST, D8O8A), Rabbit PU.1 mAb (CST, 9G7), anti-Syrian hamster IgG secondary antibody (107-606-142, Jackson ImmunoResearch) and anti-Rabbit IgG secondary antibody (Invitrogen, A-11034), as described in the Nature Research Reporting Summary. Images were obtained with BZ-II Analyzer (Keyence) and a Nikon C2 confocal microscope and analyzed by NIS-Elements AR v4.40.00 (Nikon) software.

Human synovial tissue processing, immunofluorescence staining and ChIP assay. For immunofluorescence staining, fresh synovial biopsy tissue was rinsed in cold PBS and fixed in 4% paraformaldehyde overnight for cryosection. The fixed tissue was washed twice by PBS and incubated in 30% sucrose (Sigma-Aldrich, S0389) solution for 3 h and then embedded in OCT compound (Sakura Finetek, 4583). Frozen tissue blocks were cut into 10-µm-thick sections using a cryostat (Leica), air-dried and stained with anti-human Podoplanin Antibody (BioLegend, NC-08), Rabbit ETS1 mAb (CST, D8O8A), Rabbit PU.1 mAb (CST, 9G7), Rabbit HIF2 Antibody (Novus Bio, NB100-122), anti-Rat IgG secondary antibody (Invitrogen, A-21209), anti-Rabbit IgG secondary antibody (Invitrogen, A-31573) and DAPI (Molecular Probes). Multicolor images were obtained with a Nikon C2 confocal microscope and analyzed by NIS-Elements AR v4.40.00 (Nikon) software.

For the ChIP assay, fresh synovial tissue was first subjected to synovial fibroblast isolation and the purified SFs were used for ChIP analysis. Briefly, synovial tissue was dissociated in type II collagenase solution (Worthington, LS004176; 4 mg ml^{-1}) in high-glucose DMEM (Wako, 043-30085) antibiotics (penicillin and streptomycin, Gibco, 15-140-122) at 37 °C for 1 h with frequent shaking. After the first 30-min incubation, cell suspensions were carefully homogenized by a series of 18-, 21- and 25-gauge needles until the cell suspension passed through the needles smoothly. After digestion, cells were collected by centrifugation of the culture medium (high-glucose DMEM with 10% FBS, 1% antibiotics) and the cell pellet was then treated with ACK buffer (Sigma-Aldrich, R7757) to lyse the red blood cells, and then filtered using 100-µm cell strainers to remove the tissue debris. The resulting single-cell suspensions were further subjected to synovial fibroblast purification using a BD FACSAria using the following BioLegend antibodies: anti-human CD45 (2D1), Podoplanin (NC-08), CD31(WM59) and CD146(P1H12). SFs at passage 3 or 4 were stimulated with or without 20 ng ml^{-1} TNF (R&D, 210-TA) plus 1 µM prostaglandin E2 (Cayman Chemical, 14010) for 6 h and then subjected to ChIP assay using a SimpleChIP Plus Enzymatic Chromatin IP Kit (Cell Signaling Technology, 9005). In brief, 5 µg of micrococcal nuclease digested chromatin extract was incubated with antibodies to ETS1 (D8O8A, Cell Signaling Technology) or a normal rabbit IgG antibody (2729, Cell Signaling Technology). Purification was performed according to the protocol of the SimpleChIP Plus Enzymatic Chromatin IP Kit (Cell Signaling Technology) and the bound sequences were determined by quantitative real-time PCR using the following primers: *E3*, 5′-CCTATTACGGCTGTGATCTGGAATG-3′ and 5′-AGGATGAGACGTGTGGCCAAAA-3′; *MMP13*, 5′-CACATTGCCTGCAA AATTGATCAC-3′ and 5′-AGGAAATGGCATGACATAGAGACA-3′; *MMP3*, 5′-ATGTGAGTAGCAAAAGAAGAGGTC-3′ and 5′-CGCCTATTTATTGTAG ACAAGAGG-3′.

Mouse synovial fibroblast preparation and cell culture studies. Mouse synovial tissue was disaggregated into single-cell suspensions, as described above. For the cell culture experiments, SFs purified using a BD FACSAria were cultured in the cell culture medium for three passages and then seeded onto a 48-well plate (3,000 cells per well) for the cytokine stimulation experiments. Briefly, for *Tnfsf11*, *Mmp3 and Mmp13* detection in SFs, cells were incubated with 20 ng ml^{-1} TNF (R&D, 410-MT-010) plus 1 µM prostaglandin E2 (Cayman Chemical, 14010) or 100 ng ml^{-1} OSM (R&D, 495-MO-025) in culture medium for 3 d. For in vitro osteoclastogenesis assay, bone marrow cells were cultured with arthritic SFs with TNF/prostaglandin E2 stimulation for 12 d and the TRAP^{+} MNCs were counted using a BZ-II Analyzer (Keyence) to evaluate the osteoclast formation.

For evaluation of *Tnfsf11* expression in calvaria osteoblasts, osteoblasts were first isolated from the calvaria of newborns by enzymatic digestion using the solution α-MEM (Gibco, 11900024) with 0.1% collagenase (Wako Chemicals,

038-22361) and 0.2% Dispase II (Wako Chemicals, 383-02281). The isolated osteoblasts were then incubated in α-MEM medium containing 10% FBS, 1% antibiotics and 10^{-8} M $1,25(OH)_2D_3$ (Wako Chemicals, 034-24921) for 3 d. For in vitro osteoclastogenesis assay, bone marrow cells were cultured with calvaria osteoblasts with $1,25(OH)_2D_3$ stimulation for 9 d and the $TRAP^+$ MNCs cells were counted to evaluate the osteoclast formation.

For the evaluation of *Tnfsf11* expression in lymphocytes, cells were cultured in RPMI 1640 medium containing 10% FBS and 1% antibiotics for 48 h in a flat-bottom, non-tissue-culture-treated 48-well plate pre-coated with 5 μg ml^{-1} anti-CD3ε antibody (BioLegend, 145-2C11) and 1 μg ml^{-1} anti-CD28 antibody (BioLegend, 37.51).

Flow cytometry and antibodies. Flow cytometry analysis of mouse synovial cells was performed with a FACSCanto II and a FACSAria III (BD Biosciences) and analyzed using FlowJo (TreeStar, v10.6.2) and Diva (BD Biosciences, v9.0) software. Fc blocker (anti-mouse CD16/CD32; clone 2.4G2; TONBO Biosciences) was used before staining. The following antibodies were used: anti-CD45 (30-F11), anti-CD3 (145-2C11), anti-CD11b (M1/70), anti-podoplanin (8.1.1), anti-CD31 (390), anti-CD146 (ME-9F1), anti-Notch3 (HMN3-133) and anti-CD90.2 (53-2.1). All the antibodies were purchased from BioLegend. For intracellular staining, cells were fixed and stained with ETS1 antibody (Invitrogen, JM92-32) and anti-Rabbit IgG secondary antibody (Invitrogen, A-11034) using the Transcription Factor Staining Buffer Set (eBioscience, 00-5523-00). Antibody dilution is described in the Nature Research Reporting Summary.

Quantitative RT–PCR analysis. Total RNA was extracted from isolated cells using the ReliaPrep RNA Miniprep System (Promega, Z6011) and reverse transcribed with SuperScript III (Invitrogen, Thermo Fisher Scientific, 11752-250). Quantitative PCR was performed with a LightCycler (Roche) using SYBR Green (Toyobo). The results were normalized to the *Gapdh* expression level. The primers used were: *Gapdh*, 5′-AAGGTCATCCCAGAGCTGAA-3′ and 5′-CTGCTTCACCACCTTCTTGA-3′; *Tnfsf11*, 5′-AGCCATTTGCACACCT CAC-3′ and 5′-CGTGGTACCAAGAGGACAGAGT-3′; *Mmp3*, 5′-TCATGAA CTTGGCCACTCCCT-3′ and 5′-AGGGGATGCTGTGGGAGTTC-3′; *Mmp13*, 5′-ATGGACCTTCTGGTCTTCTGGC-3′ and 5′-CTAGGGAGTGGCCAAGC TCA-3′; *Ets1*, 5′-GTGGCCAGGAGATGGGGAAA-3′ and 5′-CATGGCGTGC AGCTCTTCAG-3′.

Histomorphometric analysis. H&E, Safranin O and TRAP staining of the joint tissue sections were performed as described previously[8]. Ankle joints isolated from the STIA mice and healthy controls were fixed in 4% paraformaldehyde overnight and decalcified in Osteosoft (Merck, 101728) for 12 d at 22–24 °C, then embedded in paraffin and sectioned (5 μm). H&E staining was used to visualize inflammatory cell infiltration into the joints and synovial pannus. Safranin O (Sigma-Aldrich, S8884) staining was used to assess cartilage damage. TRAP staining was performed at 22–24 °C for 40 min, and counterstained with hematoxylin. The number of TRAP-positive osteoclasts at the synovial pannus–articular cartilage interface was evaluated using a BZ-II Analyzer (Keyence). Histopathologic scores were calculated based on the 'SMASH' recommendations[61]. Data collection was performed in a blinded manner.

Micro-computed tomography analysis. Three-dimensional micro-CT analysis was performed on the knee and ankle joints of healthy and arthritic mice. CT scanning was performed using a ScanXmate-A100S Scanner (Comscantechno). Three-dimensional microstructural image data were reconstructed, and structural indices were calculated using TRI/3D-BON software (RATOC).

Single-cell RNA-seq and data analysis. For the CIA scRNA-seq and data analysis, live synovial cells isolated from the knee joints of CIA mice ($n=3$) on day 21 after the second immunization and healthy control mice ($n=9$) were captured with the 10x Genomics Chromium system (3,000 cells assigned) and sequencing libraries were generated using a 10x Genomics Single-cell 3′ Solution (v.3) kit and then subjected to Illumina sequencing (HiSeq 4000). Alignment, quantification and aggregation of the sample count matrices were performed using the 10x Genomics Cell Ranger pipeline (v3.1.0) according to the manufacturer's protocol (GENEWIZ). Downstream computational analysis was performed using the Seurat R package (v3, v4), including the primary analysis, quality control, normalization and scaling, clustering, gene marker identification and visualization of gene expression, as described previously[62]. Briefly, cells with fewer than 200 genes or greater than 8% mitochondrial reads or more than 7,500 nFeature_RNA were excluded. The genes expressed in fewer than three cells were also not included in the analysis. After filtering, per-cell counts were normalized, the 2,000 most variable genes were identified, and the expression levels of these genes were scaled (scale factor of 10,000) before performing principal-component analysis. For the synovial cell subtypes visualization, we retained the first ten principal components for UMAP projection and clustered at a resolution of 0.04 through a standard graph-based clustering approach and modularity optimization technique. FeaturePlot with default settings was used to visualize single cells on a UMAP plot based on gene expression. Cell clusters marked by *Ptprc* (*Cd45*), *Cdh5* and *Mcam* (*Cd146*) along with minor cell populations such as *Hapln1*$^+$ chondrocytes, *Pdpn*$^-$*Fap*$^-$*Sparc*$^+$ osteoblasts, *Plp1*$^+$ nerve cells and red blood cells were excluded for the synovial fibroblast (*Fap*$^+$*Pdpn*$^+$) analysis. For the synovial fibroblast ($n=243$) analysis, 20 principal components were used for graph-based clustering (resolution of 0.5), and UMAP dimensionality reduction was computed. Differential gene expression analysis and visualization of gene expression were performed using Seurat functions with default parameters. Regulatory target gene-set analysis was performed using Molecular Signatures Database v7.4 (MSigDB) C3 datasets (https://www.gsea-msigdb.org/gsea/msigdb/index.jsp) with VISION (v2.1.0) R package[63].

For the RA patient synovial cells data analysis, we analyzed two datasets[15,16] (dbGaP Study Accession phs001529.v1.p1 and ImmPort SDY998) using Seurat v.3 (the same pipeline as in the mouse data analysis unless otherwise indicated) and the synovial fibroblast transcriptomic data were integrated for downstream analysis utilizing the SCTransform workflow as described in Seurat v3 Integration. Briefly, SFs from each dataset were first computationally selected based on the lack of expression of *PTPRC* (encoding CD45) and the expression of *FAP* (encoding fibroblast activation protein) and *PDPN* (encoding podoplanin) and were integrated using functions compatible with SCTransform normalization[64]. Subsequent graph-based clustering was performed at a resolution of 0.5. Violin plots in Seurat functions were used to visualize the selective gene expressions with the default parameters. Cross-tissue fibroblast atlas datasets[4] (https://www.fibroxplorer.com/) were utilized to visualize ETS1, TNFSF11, MMP3 and MMP13 expression levels across tissues and diseases. Single-cell analyses of ulcerative colitis[34] (SCP259) and colorectal cancer fibroblasts[35] (GSE178341) were performed using Single Cell Portal (https://singlecell.broadinstitute.org/single_cell/) with default settings.

Data of human breast cancers[38] (GSE176078), DSS-induced colitis[43] (GSE172261), liver cirrhosis[49] (GSE136103), pulmonary fibrosis[50] (GSE135893) and kidney fibrosis[51] (GSE140023) were retrieved from the Gene Expression Omnibus (GEO) dataset and further processed and analyzed using Seurat (v3, v4) in a standard way. Clustering and cell-type annotation were based on the authors' descriptions in the original papers and deposited codes.

Bulk RNA-seq. SFs were isolated from the inflamed synovial tissue of day-16 STIA mice as described above. Total RNA was extracted from isolated cells using the RNeasy Kit (QIAGEN, 74104). Complementary DNA was synthesized and amplified using SMART-seq v.4 Ultra Low Input RNA Kit for Sequencing (Clontech Laboratories), then subjected to Ion Proton sequencer (Thermo Fisher Scientific) and further processed using CLC genomics Workbench v12.0.3. The differential gene expression analysis and pathway enrichment analysis were performed using DESeq2 R package (v1.34.0), pheatmap (v1.0.12) R package and the BioJupies tool (https://maayanlab.cloud/biojupies/).

ChIP–seq, ATAC–seq, Hi-C and bulk RNA-seq data analysis. Raw H3K27ac ChIP–seq (GSE128642) and ATAC–seq (GSE128644)[19] data were downloaded and the following analysis was performed. Quality control of the ChIP–seq reads was carried out with fastp (version 0.20.1) using the following parameters: --3 --5 --W 4 --M 20 --w4 --q 30 --n 5 --l 25. The reads were then mapped to reference the human genome (hg19) with bowtie2 (version 2.3.5.1) using the default parameters. Blacklist regions (https://www.nature.com/articles/s41598-019-45839-z/) were removed from[65] the analysis. Peak calling was performed with MACS2 (version 2.2.7.1) using the following parameters: --g 2.8e+9, --q 0.01 and --keep-dup all. BRD4 and Pol II ChIP–seq data (GSE148399), H3K4me3, H3K27ac ChIP–seq and Hi-C data (NBDC accession code hum0207) were downloaded from the GEO and the NBDC Human Database and visualized with Integrative Genomics Viewer (v2.7.0). ETS1 ChIP–seq data of fibroblasts derived from various tissues were downloaded from the ENCODE Project database (ENCFF614VLL, ENCFF982OBR, ENCFF577JGN, ENCFF169ARY, ENCFF244ZNY, ENCFF569PTY, ENCFF523ZCW, ENCFF213MVM, ENCFF383CFQ and ENCFF314JXH). The representative ETS1 ChIP–seq data shown in Fig. 3f,g (ENCFF614VLL, lung fibroblasts) were visualized on the *MMP13* and *MMP3* loci. Sequence similarity between humans and other vertebrates and the homologous regions of E1–E5 in the mouse genome were analyzed with the ECR Browser[66] (https://ecrbrowser.dcode.org/) based on sharing at least 60% sequence identity across 100-base-pair ECR length. For motif analysis, we used HOMER (v4.8) to analyze the transcription factor binding motifs that were enriched in RANKL enhancers under ATAC–seq peaks. The sequences were compared to random genomic fragments of the same size and normalized for G+C content to identify the motifs for which the targeted sequences showed enrichment. Motif from the JASPAR database was identified by running HOMER on the hg19 reference. We performed the enrichment analysis of the transcription factor binding sites using the JASPAR CORE collection database (https://jaspar.genereg.net/). Mouse data analyses and visualization were performed in a similar manner to that described above. The datasets H3K27ac ChIP–seq (GSE54782, GSE123198, GSE145951 and GSE155882) and ATAC–seq (BioProject PRJNA643827) were downloaded and visualized in the *Tnfsf11* locus (mm9).

For the bulk RNA-seq dataset NBDC hum0207 and GSE148395, GSE129451 (refs. [14,20,24]), GSE166927 (ref. [67]) and GSE166925 (ref. [67]) data analyses, the

normalized gene count files were retrieved for further gene expression analysis. The data of PDPN$^+$FAP$^+$ SFs in GSE129451 and GSE166925 were extracted and transformed into $\log_{10}$ as the expression levels of the indicated genes for Spearman's correlation analysis. Standardized RNA-seq expression and clinical annotation data for pancreatic adenocarcinoma (TCGA, PanCancer Atlas, 184 samples), adult soft tissue sarcomas (TCGA, Cell 2017, 206 samples), mesothelioma (TCGA, PanCancer Atlas, 87 samples), lung adenocarcinoma (TCGA, Firehose Legacy, 586 samples), colon cancer (CPTAC-2 Prospective, Cell 2019, 110 samples) and colorectal adenocarcinoma (TCGA, Nature 2012, 276 samples) datasets were analyzed using cBioPortal analysis[68] (https://www.cbioportal.org/). The results shown here are in whole or in part based upon data generated by the TCGA Research Network (https://www.cancer.gov/tcga/).

Reporter assay. The mouse *Tnfsf11* promoter luciferase construct pGL3-2K was previously described[57]. The enhancer constructs (pGL3-E1 to pGL3-E5) used in this experiment were created by insertion of the homologous sequence elements of E1–E5 (GRCm39 mouse Chr. 14: E1, 78,560,777–78,563,598; E2, 78,613,530–78,616,951; E3, 78,653,941–78,655,122; E4, 78,668,568–78,672,548; E5, 78,695,879–78,697,602) upstream of the minimal *Tnfsf11* promoter, which was generated from pGL3-2K. The cDNA fragment encoding ETS1 was amplified by PCR and sub-cloned into the pcDNA3.1 expression vector resulting in the expression plasmid ETS1. These procedures were performed according to the In-Fusion HD Cloning Kit (Takara Bio, 639650) manufacturer's protocol (detailed protocols are available upon request). All plasmids created in this study were sequenced to verify successful cloning. The individual enhancer constructs (pGL3-E1 to pGL3-E5), *Tnfsf11* promoter pGL3-2K and expression plasmid ETS1 along with the *Renilla*-expressing control plasmid (phRG-TK) (Promega) were transfected into HEK293T cells using Lipofectamine 3000 reagent (Invitrogen, L3000015). After 48 h, dual-luciferase assay was performed according to the manufacturer's instructions in the Dual-luciferase Reporter Assay System (Promega, E1910).

GWAS data analysis. We extracted 29 variants within the *ETS1* region (Chr. 11: 128,957,453–127,828,656 in hg19), which exceeded the genome-wide significance threshold ($P < 5 \times 10^{-8}$) established in a previously performed GWAS for RA[27]. We checked the overlap between the ChIP–seq peaks and the RA-associated variants using Bedtools (v2.29.2, https://github.com/arq5x/bedtools2/). To check the overlap between the candidate *cis*-regulatory element (https://screen.encodeproject.org/) based on hg38 and the RA-associated variants with Bedtools, we used LiftOver (https://genome.ucsc.edu/cgi-bin/hgLiftOver/).

Statistical analyses. Data were analyzed on GraphPad Prism software v8.4.0 and R software v4.1.2. The statistical tests, *n* values, replicate experiments and *P* values are all indicated in the figures and/or legends. *P* values were calculated using Student's *t*-test, Mann–Whitney *U* test, logrank test and ANOVA with Tukey's post hoc test or Sidak's multiple-comparisons test. Statistical analyses of bulk RNA-seq were independently performed using the DESeq2 R package, BioJupies and cBioPortal tools as indicated in figure legends and/or the Methods.

Reporting summary. Further information on research design is available in the Nature Research Reporting Summary linked to this article.

Data availability

All the data that support the plots within this paper are available in the main text or in the Supplementary Information. The scRNA-seq data and bulk RNA-seq data produced in this study are available in the public GEO database under accession codes GSE192504 and GSE201310. The referenced publicly available datasets were downloaded from the GEO, BioProject NCBI database, ENCODE Project database, TCGA database, National Bioscience Database Center (NBDC) database and MSigDB Collections C3 datasets: regulatory target gene sets (legacy transcription factor targets, https://www.gsea-msigdb.org/gsea/msigdb/index.jsp). scRNA-seq (dbGaP study accession phs001529.v1.p1, ImmPort SDY998, GSE178341, SCP259, GSE176078, GSE136103, GSE135893, GSE140023 and GSE172261), ChIP–seq (GSE128642, GSE148399, GSE54782, GSE123198, GSE145951 and GSE155882; ENCODE: ENCFF614VLL, ENCFF982OBR, ENCFF577JGN, ENCFF169ARY, ENCFF244ZNY, ENCFF569PTY, ENCFF523ZCW, ENCFF213MVM, ENCFF383CFQ and ENCFF314JXH), ATAC–seq (GSE128644 and BioProject PRJNA643827), Hi-C (NBDC hum0207), bulk RNA-seq (GSE129451 and GSE148395; NBDC hum0207; GSE166927 and GSE166925), TCGA clinical data and sequencing data (pancreatic adenocarcinoma (PanCancer Atlas), adult soft tissue sarcomas, mesothelioma (PanCancer Atlas), lung adenocarcinoma (Firehose Legacy) and colon cancer CPTAC-2 prospective and colorectal adenocarcinoma). Source data are provided with this paper.

Code availability

R scripts for data analysis used in this study are available at GitHub (https://github.com/MingluYAN).

References

60. Fukushima, K. et al. Dysregulated expression of the nuclear exosome targeting complex component Rbm7 in nonhematopoietic cells licenses the development of fibrosis. *Immunity* **52**, 542–556 (2020).
61. Hayer, S. et al. 'SMASH' recommendations for standardised microscopic arthritis scoring of histological sections from inflammatory arthritis animal models. *Ann. Rheum. Dis.* **80**, 714–726 (2021).
62. Tsukasaki, M. et al. Stepwise cell fate decision pathways during osteoclastogenesis at single-cell resolution. *Nat. Metab.* **2**, 1382–1390 (2020).
63. DeTomaso, D. et al. Functional interpretation of single cell similarity maps. *Nat. Commun.* **10**, 4376 (2019).
64. Hafemeister, C. & Satija, R. Normalization and variance stabilization of single-cell RNA-seq data using regularized negative binomial regression. *Genome Biol.* **20**, 296 (2019).
65. Amemiya, H.M., & Boyle, A.P. The ENCODE Blacklist: Identification of Problematic Regions of the Genome. *Sci. Rep.* **9**, 9354 (2019).
66. Ovcharenko, I., Nobrega, M. A., Loots, G. G. & Stubbs, L. ECR Browser: a tool for visualizing and accessing data from comparisons of multiple vertebrate genomes. *Nucleic Acids Res.* **32**, W280–W286 (2004).
67. Friedrich, M. et al. IL-1-driven stromal–neutrophil interactions define a subset of patients with inflammatory bowel disease that does not respond to therapies. *Nat. Med.* **27**, 1970–1981 (2021).
68. Cerami, E. et al. The cBio cancer genomics portal: an open platform for exploring multidimensional cancer genomics data. *Cancer Discov.* **2**, 401–404 (2012).

Acknowledgements

We thank A. Terashima, T. Asano, T. Sugita, H. Urabe, S. Yin, W. Yin, S. Zang, K. Kusubata, A. Suematsu, K. Kubo, Y. Omata, N. Kamiya, M. Hatakeyama, M. Miyoshi, G. Zhao, K. Ohmura, J. Nishio and K. Nakano for thoughtful discussion and valuable technical assistance. We appreciate the great contribution of K. Onimaru for the data analysis. This work was supported in part by the Japan Agency for Medical Research and Development (AMED) under grant number JP22ek0410073, AMED-CREST under grant number JP22gm1210008 and AMED-PRIME under grant number JP22gm6310029h0001; Japan Society for the Promotion of Science (JSPS): Grants-in-Aid for Specially Promoted Research (15H05703), Scientific Research S (21H05046), Scientific Research B (21H03104 and 22H02844) and Challenging Research (20K21515 and 21K18254). M.Y. was supported by a JSPS Research Fellowship for Young Scientists (19J21942) and a JSPS Postdoctoral Fellowships for Overseas Researchers (22F22108).

Author contributions

M.Y. conceived the project and performed most of the experiments and data analyses, interpreted the results and wrote the manuscript. N.K., Y.O., H.I.S., H. Takaba, W.P. and T.N. provided advice on project planning and contributed to data interpretation and manuscript preparation. R.M. constructed the enhancer plasmids, performed reporter assay experiment and contributed to data interpretation. N.C.-N.H. and Y.T. performed computational analyses and contributed to data interpretation. R.K. and S.K. constructed and provided RANKL promoter luciferase plasmid and provided advice on project planning and data interpretation. Y.M., T.S. induced fibrosis model, performed the histological analysis and provided advice on data interpretation. T.O., S.-H.I., C.J.K. contributed to the generation of genetically modified mice and provided advice on data interpretation. G.K. generated and provided the *Col6a1*-Cre mice, advised on epigenomic data analysis and provided a thoughtful discussion on data interpretation. S.T. advised on project planning, provided the human synovium specimens and a thoughtful discussion on data interpretation. K.O. provided advice on project planning, immunostaining and histological analysis, data interpretation and manuscript preparation. M.T. supervised project planning and data interpretation and wrote the manuscript. H. Takayanagi directed the project and wrote the manuscript.

Competing interests

The Department of Osteoimmunology is an endowed department supported by unrestricted grants from AYUMI Pharmaceutical, Chugai Pharmaceutical, MIKI HOUSE and Noevir. S.-H.I. is the CEO of the ImmunoBiome but declares no competing interests for this paper. The remaining authors declare no competing interests.

Additional information

Extended data is available for this paper at https://doi.org/10.1038/s41590-022-01285-0.

Supplementary information The online version contains supplementary material available at https://doi.org/10.1038/s41590-022-01285-0.

Correspondence and requests for materials should be addressed to Hiroshi Takayanagi.

Peer review information *Nature Immunology* thanks Christopher Buckley and Caroline Ospelt for their contribution to the peer review of this work. Primary Handling Editor: L. A. Dempsey, in collaboration with the *Nature Immunology* team.

Reprints and permissions information is available at www.nature.com/reprints.

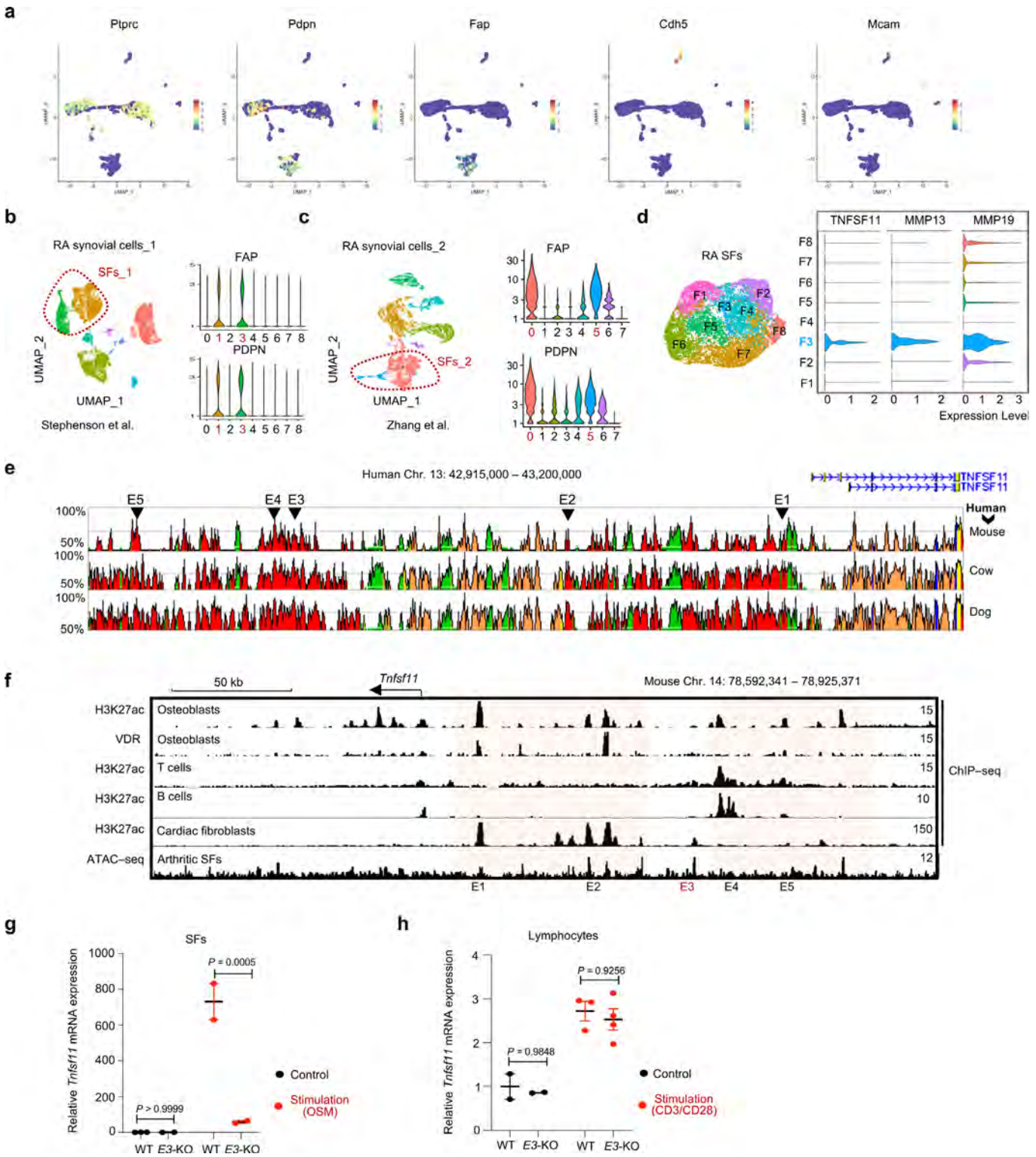

Extended Data Fig. 1 | See next page for caption.

Extended Data Fig. 1 | A distal enhancer regulates RANKL gene expression in arthritic SFs. a, The expression pattern of representative cell-type marker genes in the CIA synovial cells (n = 2,160) in the UMAP visualization. The feature plots of the expression distribution of the major cell-type marker genes corresponding to the assigned cell types shown in (Fig. 1a). **b, c**, UMAP plots and unsupervised clustering of the synovial cells of individuals with RA **(b)** dbGaP Study Accession: phs001529.v1.p1, n = 19,599 cells; **(c)** ImmPort Accession: SDY998, n = 9,553 cells) colored by cluster. The violin plots on the right sides show the expression of the known SF marker genes. **d**, UMAP plot of the integrated SFs (n = 11,188 cells) from RA. Eight clusters (F1-F8) identified through unsupervised graph-based clustering are shown in color. Violin plots show the expression of selected genes in the SF sub-clusters. **e**, The sequence similarity of E1-E5 between humans and other vertebrates analyzed by the ECR Browser. The homologous sequence regions of E1-E5 in the mouse genome are indicated by arrows. **f**, Epigenomic analyses at the *Tnfsf11* locus (mm9) in osteoblasts (vitamin D_3 stimulation followed by H3K27ac ChIP-seq and vitamin D receptor (VDR) ChIP-seq (GSE54782)), in T cells (anti-CD3/CD28 antibody stimulation followed by H3K27ac ChIP-seq (GSE123198)), in B cells (IL-2/IL-4/IL-5/CD40L stimulation followed by H3K27ac ChIP-seq (GSE145951)), in cardiac fibroblasts (TGFβ stimulation followed by H3K27ac ChIP-seq (GSE155882)), in arthritic SFs (TNF stimulation followed by ATAC-seq, PRJNA643827)). **g, h**, The expression levels of *Tnfsf11* mRNA in arthritic SFs (WT: control, n = 3; stimulation, n = 2; E3-KO: control: n = 2; stimulation, n = 2) and lymphocytes (WT: control, n = 2; stimulation, n = 3; E3-KO: control: n = 2; stimulation, n = 4). Data were expressed as mean ± s.e.m. *P* values were determined by two-way ANOVA analysis followed by Turkey's post hoc test.

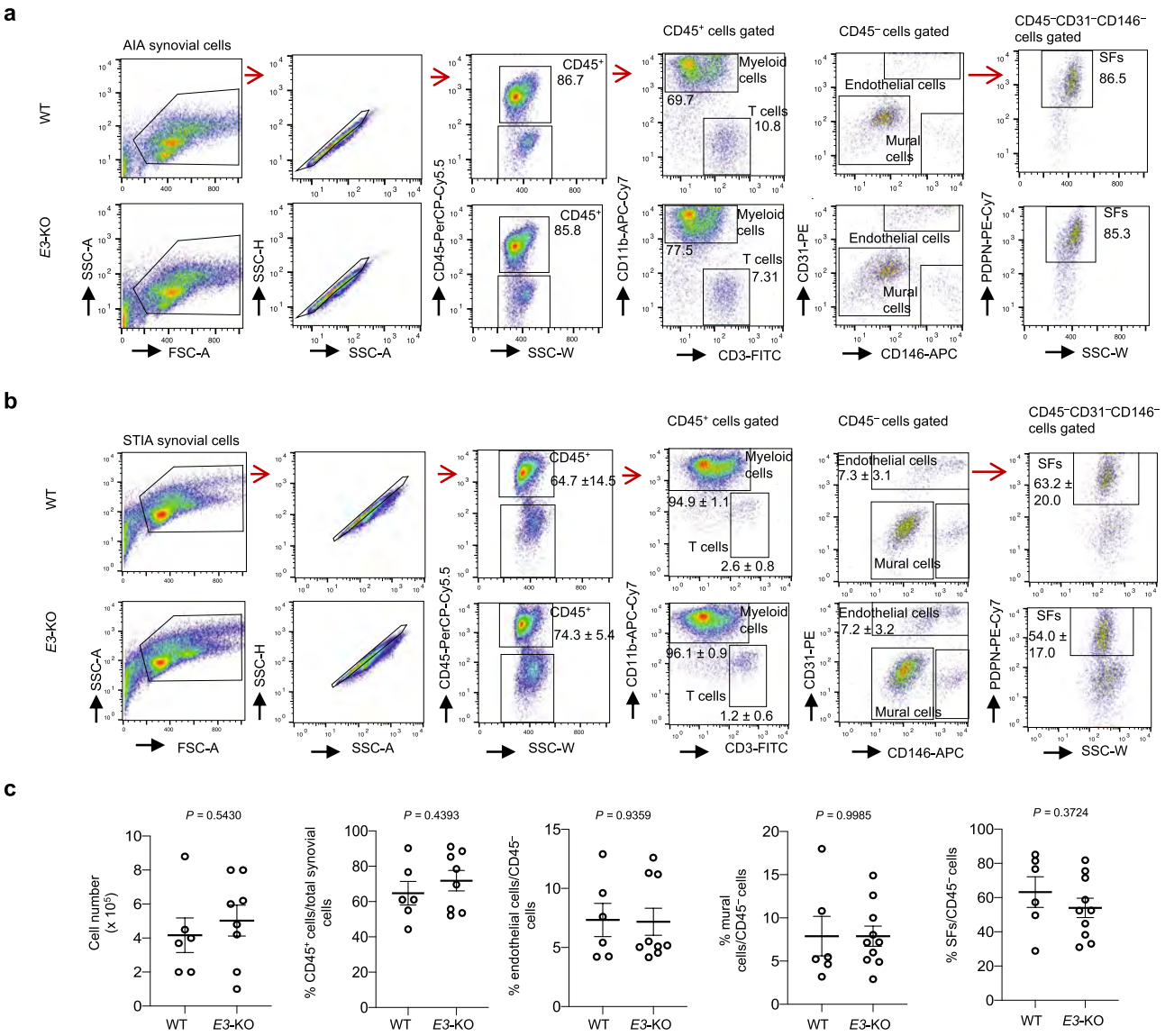

Extended Data Fig. 2 | E3 deletion ameliorates arthritis-induced bone damage. a, Flow cytometry gating strategies and a representative FACS plot of synovial cells from WT and *E3*-KO AIA (day 7 after intra-articular injection) mice, the number shows a frequency of indicated population from more than three independent experiments. **b**, Flow cytometry gating strategies and a representative FACS plot of synovial cells from WT and *E3*-KO STIA (day 10) mice (n = 6-10), data were expressed as mean ± s.e.m. **c**, Synovial cell number per inflamed joint (WT, n = 6; E3-KO, n = 8) and the frequencies of $CD45^+$ cells (WT, n = 6; E3-KO, n = 8), endothelial cells (WT, n = 6; E3-KO, n = 9), mural cells (WT, n = 6; E3-KO, n = 10), SFs (WT, n = 6; E3-KO, n = 10). Data were expressed as mean ± s.e.m. *P* values were determined by two-tailed *t*-test.

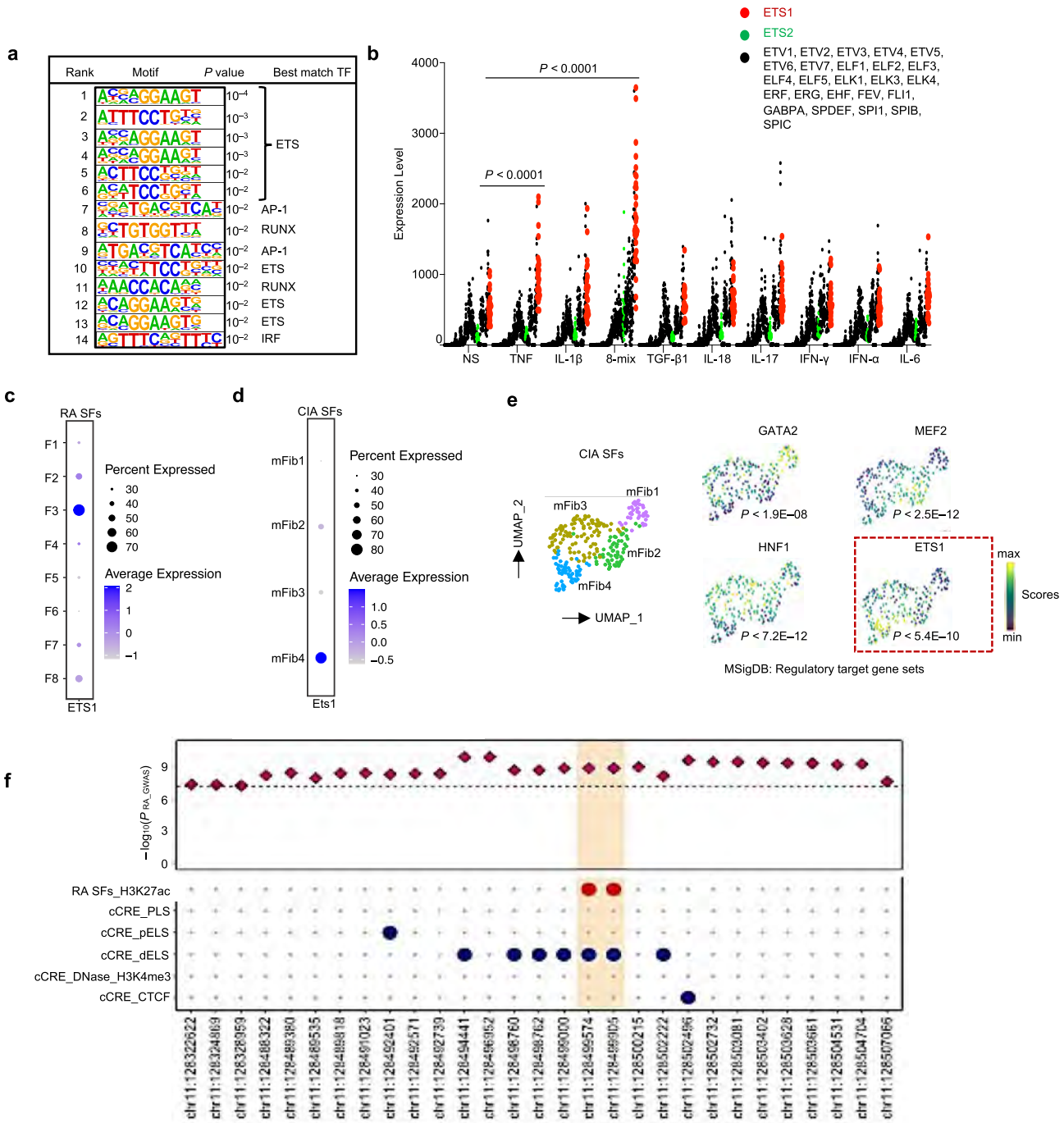

Extended Data Fig. 3 | ETS1 regulates the expression of tissue-destructive genes in SFs. a, Motif enrichment analysis in RANKL enhancers by HOMER software (*P* values: hypergeometric test) **b**, The expression levels of ETS family members in RA patients-derived SFs under the indicated conditions (NBDC accession code hum0207). Data were expressed as mean ± s.e.m. *P* values were determined by one-way ANOVA analysis followed by Turkey's post hoc test. **c, d**, The expression levels of ETS1 in RA patient-derived SF sub-clusters F1 to F8 **(c)** and CIA SFs sub-clusters mFib1 to mFib4 **(d)**. **e**, Regulatory target gene sets analysis in CIA SFs sub-clusters using MSigDB C3 datasets (legacy transcription factor targets) performed with VISION R package (*P* values: Wilcoxon rank-sum test). **f**, Alignment of the *ETS1* variants associated with RA. The upper panel shows the *P*-values of the 29 variants within the *ETS1* region (Chr. 11: 127,828,656-128,957,453 in hg19) which exceeded the genome-wide significance threshold ($P < 5 \times 10^{-8}$) in a previously performed RA GWAS study[27]. The dashed line indicates the genome-wide significance threshold ($P < 5 \times 10^{-8}$). The lower panel (from top to bottom) shows the H3K27ac ChIP-seq (GSE128642) peaks detected in RA patient SFs, candidate *cis*-regulatory element (cCRE) with promoter-like signatures (cCRE_PLS), cCRE with proximal enhancer-like signatures (cCRE_pELS), cCRE with distal enhancer-like signatures (cCRE_dELS), cCRE enriched with DNase and H3K4me3 signals (cCRE_DNase_H3K4me3) and cCRE enriched with CTCF signals (cCRE_CTCF). Overlapping of the RA-associated *ETS1* variants with the H3K27ac ChIP-seq (GSE128642) peaks detected in RA patient SFs and the candidate cCRE are indicated. The red-colored dots (ChIP-seq) and blue-colored dots (cCRE) represent overlaps. The shaded area indicates the overlap among the RA-associated *ETS1* variants, and the H3K27ac peaks detected in RA patient SFs and cCRE.

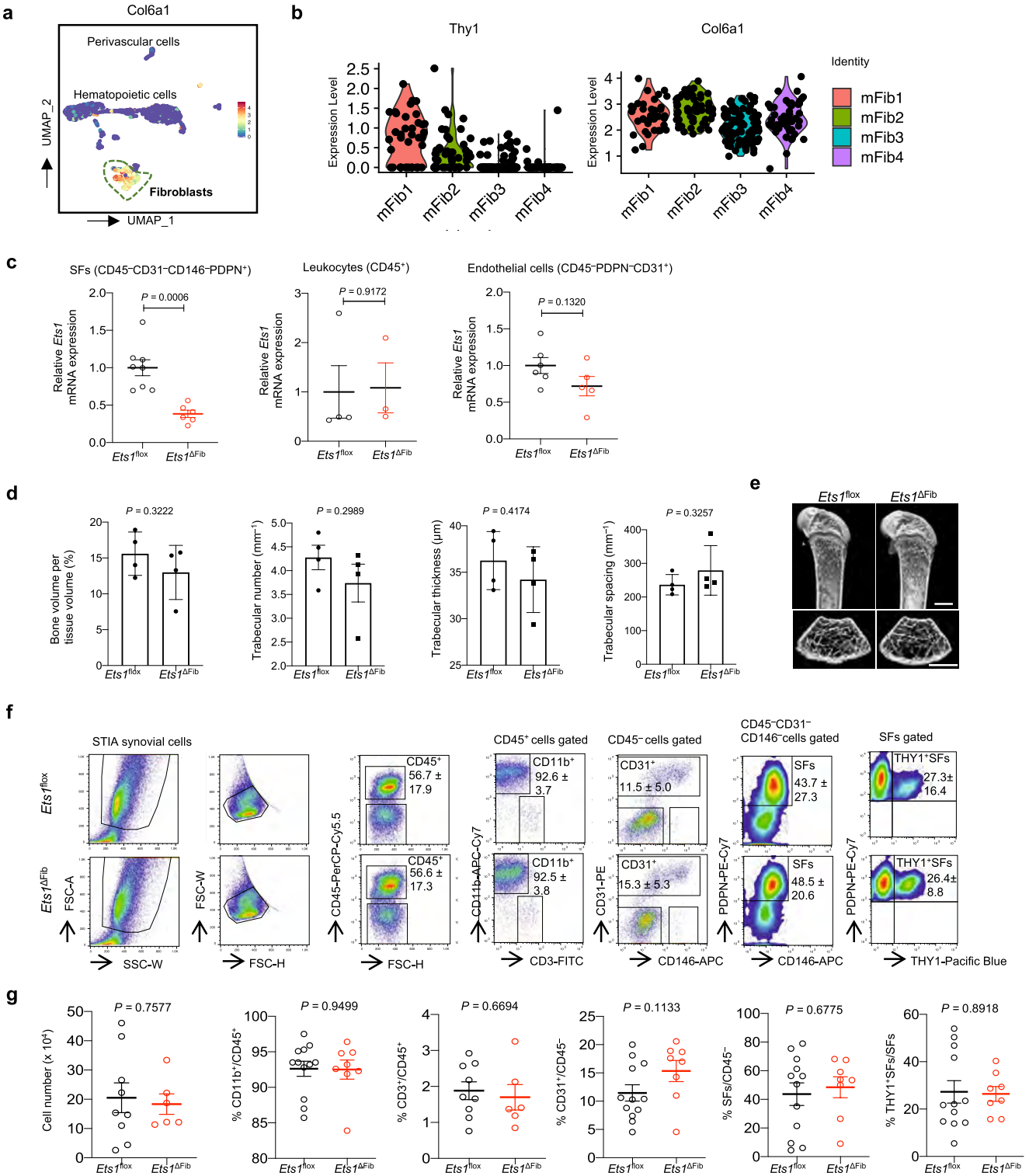

Extended Data Fig. 4 | ETS1 deletion in SFs attenuates arthritis-induced joint damage. a, The expression of Col6a1 in the CIA synovial cells (n = 2,160) in the UMAP visualization. **b**, Violin plots showing the expression of Thy1 and Col6a1 in the SF sub-clusters. **c**, The expression levels of *Ets1* mRNA in sorted SFs (*Ets1*^{flox}, n = 8; *Ets1*$^{\Delta Fib}$, n = 6), leukocytes (*Ets1*^{flox}, n = 4; *Ets1*$^{\Delta Fib}$, n = 3) and endothelial cells (*Ets1*^{flox}, n = 6; *Ets1*$^{\Delta Fib}$, n = 5) of the inflamed synovium. Data were expressed as mean ± s.e.m. *P* values were determined by two-tailed *t*-test. **d, e**, Parameters of the micro-CT analysis (bone volume per tissue volume, trabecular number, trabecular thickness and trabecular spacing) of the femurs of *Ets1*^{flox} and *Ets1*$^{\Delta Fib}$ mice (female, n = 4 per group) at the age of 8 weeks under physiological conditions. Data were expressed as mean ± s.e.m. *P* values were determined by two-tailed *t*-test (**d**). Representative micro-CT images (female, 8 weeks). Micro-CT scale bars: 1mm (**e**). **f, g**, Representative FACS plot and gating strategies of STIA (day 16) synovial cells from *Ets1*^{flox} and *Ets1*$^{\Delta Fib}$ mice, n = 6-12 (**f**). Synovial cell number per inflamed joint and the frequencies of CD3$^+$ cells (*Ets1*^{flox}, n = 9; *Ets1*$^{\Delta Fib}$, n = 6), and the frequencies of the other cell types in synovial tissue of *Ets1*^{flox} mice (n = 12) and *Ets1*$^{\Delta Fib}$ STIA mice (n = 8). Data were expressed as mean ± s.e.m. *P* values were determined by two-tailed *t*-test (**g**).

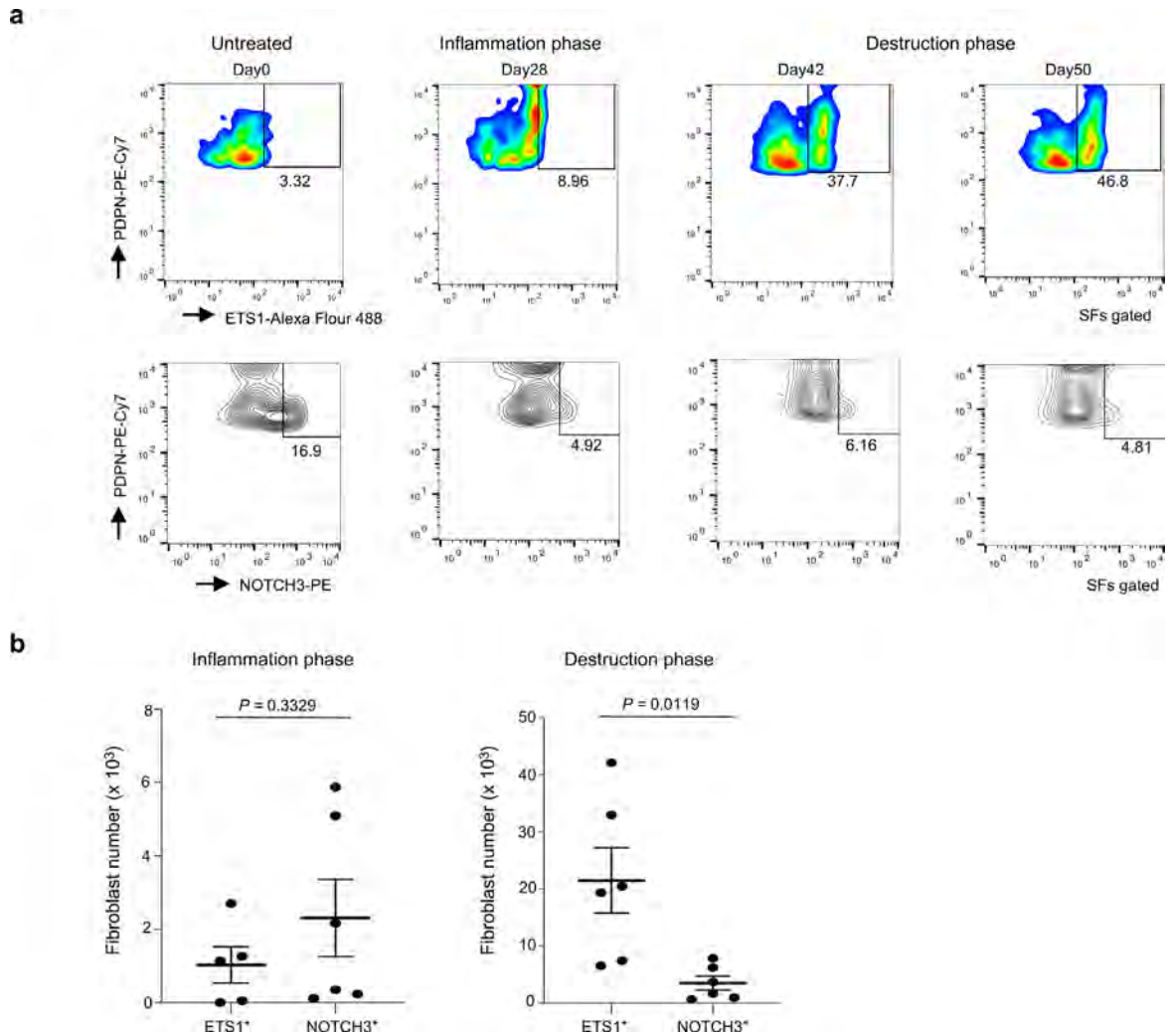

Extended Data Fig. 5 | ETS1⁺ SFs increased in number in the destruction phase during CIA. a, Representative FACS plot of SFs derived from the mice of untreated control and CIA (inflammation phase: day 28; destruction phase: day 42 to day 50). **b**, Quantification of the cell number of ETS1⁺ fibroblasts of n = 5 mice in inflammation phase, n = 6 mice in destruction phase and NOTCH3 + fibroblasts of n = 6 mice in inflammation phase, n = 6 mice in destruction phase in the joints. Data were expressed as mean ± s.e.m. *P* values were determined by two-tailed *t*-test.

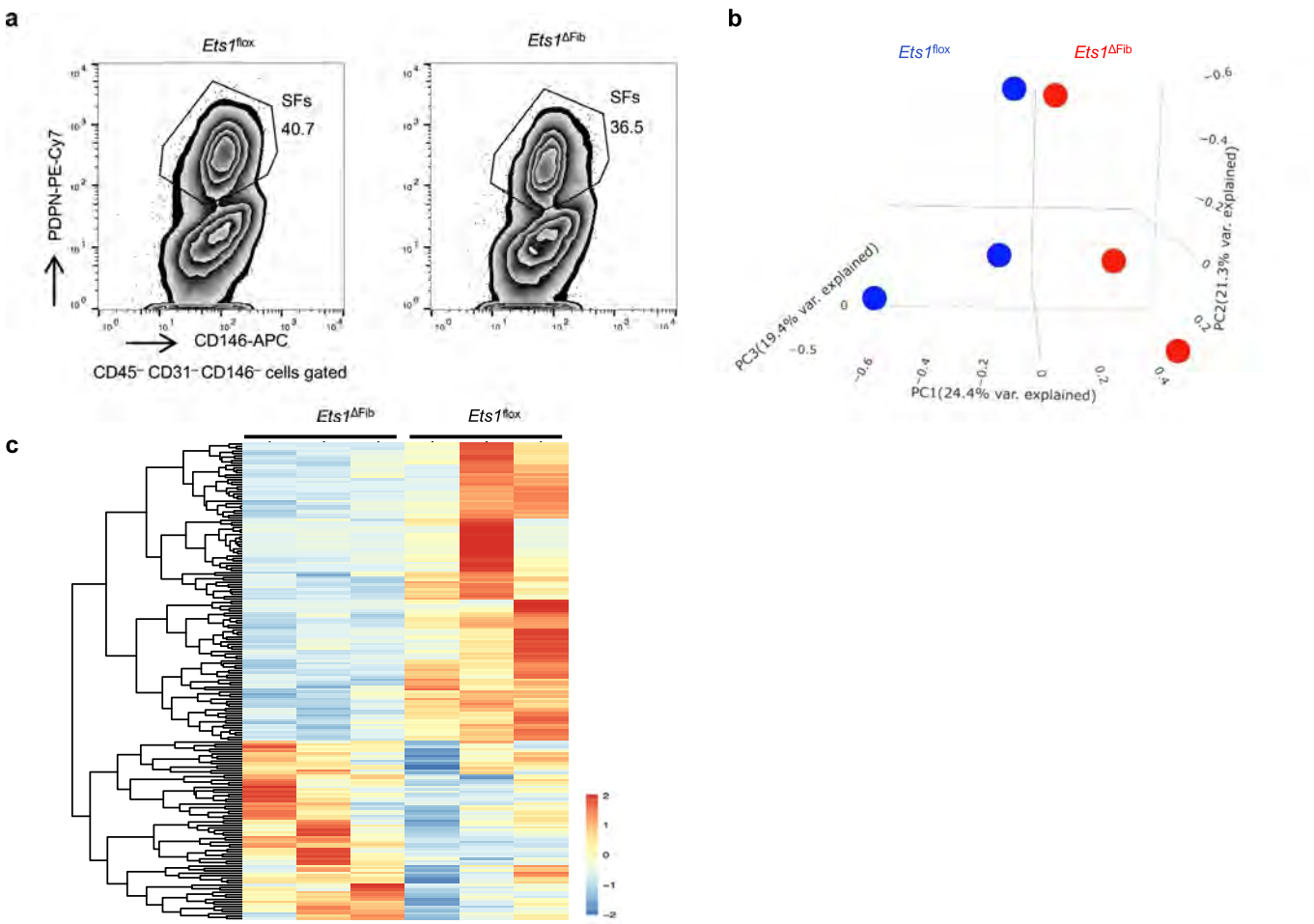

Extended Data Fig. 6 | RNA-seq analysis of *Ets1*-deleted fibroblasts. a, Representative FACS plot of SFs (STIA day 16) from *Ets1*^{flox} and *Ets1*$^{\Delta Fib}$ mice, n = 3. **b**, Three-dimensional PCA analysis for the top 2500 variable genes in SFs derived from *Ets1*^{flox} and *Ets1*$^{\Delta Fib}$ mice, n = 3. **c**, Heat map showing the DEGs between *Ets1*^{flox}- and *Ets1*$^{\Delta Fib}$-SFs. (DEGs: $\log_2$ FC > 0.5, $P < 0.05$ determined by DESeq2 (Wald test with Benjamini and Hochberg method correction)).

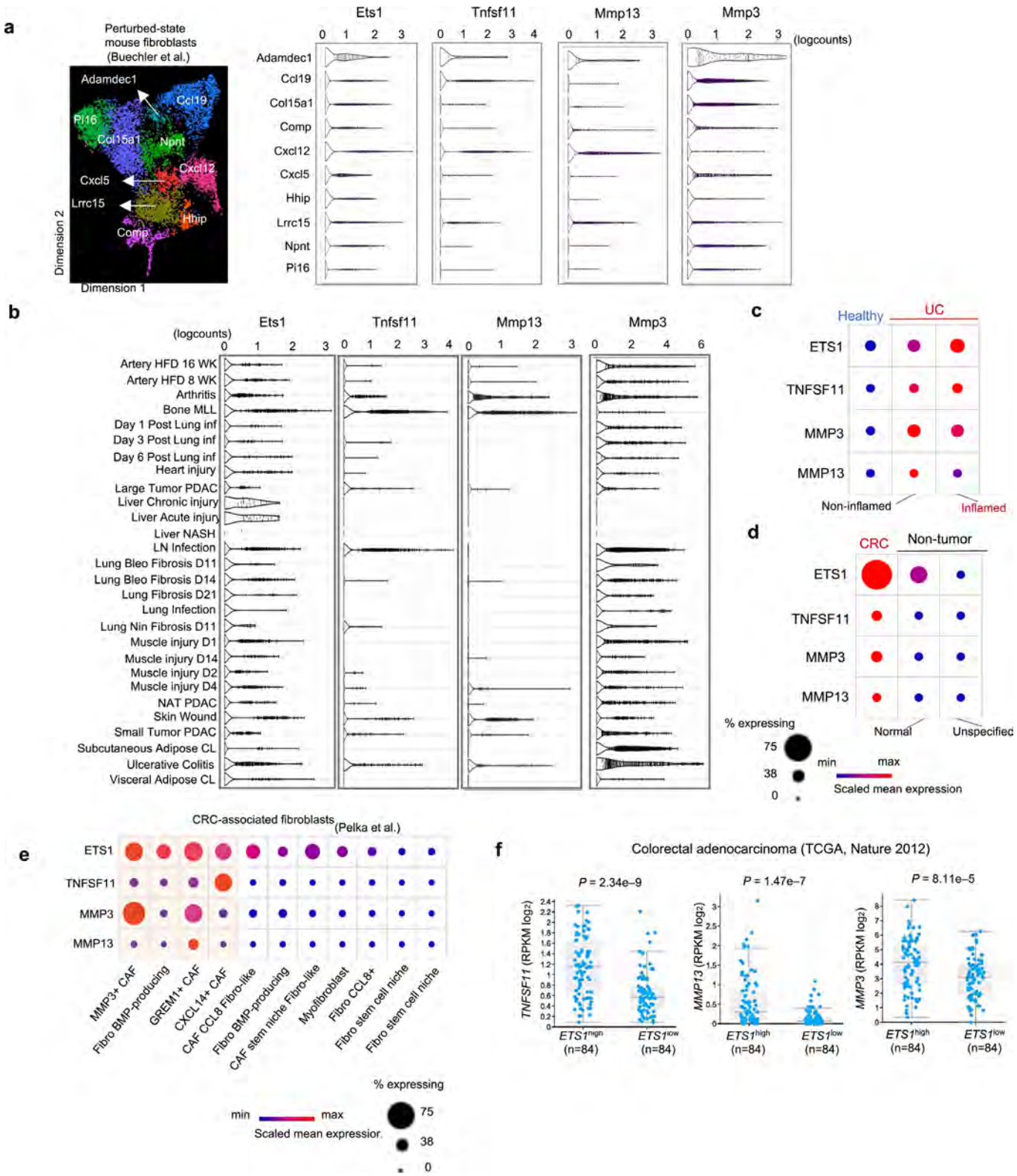

Extended Data Fig. 7 | See next page for caption.

Extended Data Fig. 7 | Cross-tissue analysis of fibroblast scRNA-seq datasets. a, b, Mouse perturbed-state fibroblasts atlas[4] and the expression of Ets1, Tnfsf11, Mmp13 and Mmp3 in the identified clusters (a) colored by Adamdec1 logcounts and in the fibroblast cells across diseases (b) (https://www.fibroxplorer.com/home). **c**, Dot plot showing the expression of ETS1, TNFSF11, MMP3 and MMP13 in ulcerative colitis (UC)-associated stromal cells and healthy controls (SCP259). **d**, Dot plot showing the expression of ETS1, TNFSF11, MMP3 and MMP13 in stromal cells of tumor tissues and adjacent normal colon tissues of CRC patients (GSE178341). **e**, Dot plot showing the expression of ETS1, TNFSF11, MMP3 and MMP13 across CRC-associated fibroblast clusters (GSE178341). **f**, Expression levels of TNFSF11, MMP13, MMP3 in TCGA datasets of CRC patients. Groups were split by the expression levels of ETS1 (top third $ETS1^{high}$, n = 84; bottom third $ETS1^{low}$, n = 84). Box plots (center: median; limits: upper 75^{th} percentile, lower: 25^{th} percentile); whiskers were drawn independently above and below the box and extended to the maximum and minimum values (1.5*interquartile range, points were outliers). *P* values were calculated by two-tailed Student's t-test.

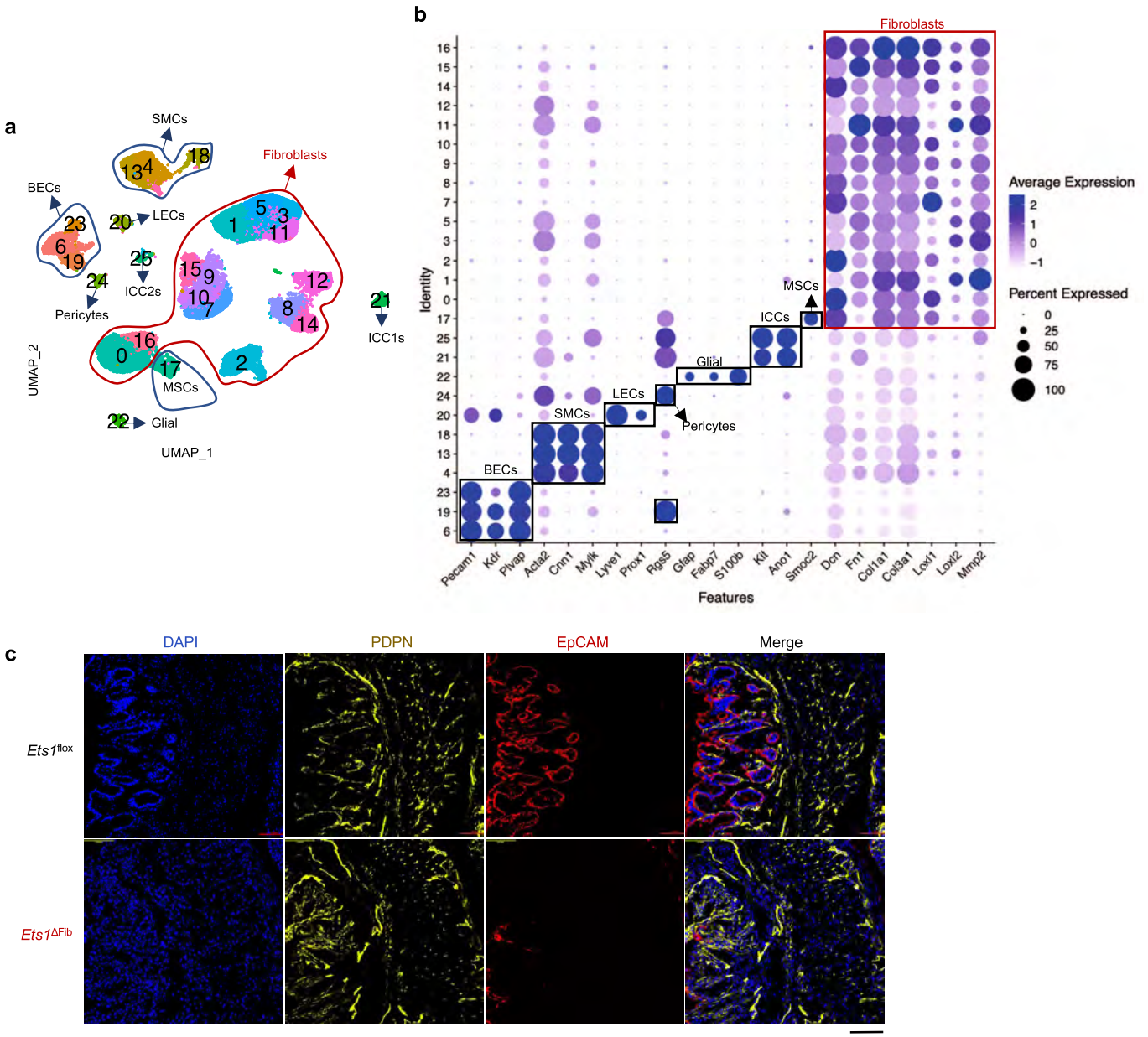

Extended Data Fig. 8 | *Ets1*-expressing fibroblasts contribute to mucosal remodeling in colitis. a, UMAP embedding of 34,197 mesenchymal cells derived from colon tissues (GSE172261) of DSS-fed mice colored by cluster. SMCs: smooth muscle cells, BECs: blood endothelial cells, LECs: lymphatic endothelial cells, ICCs: interstitial cells of Cajal, MSCs: mesenchymal stem cells. **b**, Dot plot showing the expression of representative cell-type marker genes for cell type annotation in (a). **c**, Representative immunofluorescence images of colons derived from *Ets1*^{flox} and *Ets1*$^{\Delta Fib}$ mice after DSS administration (day 10), n = 3. Scale bar: 100 μm.

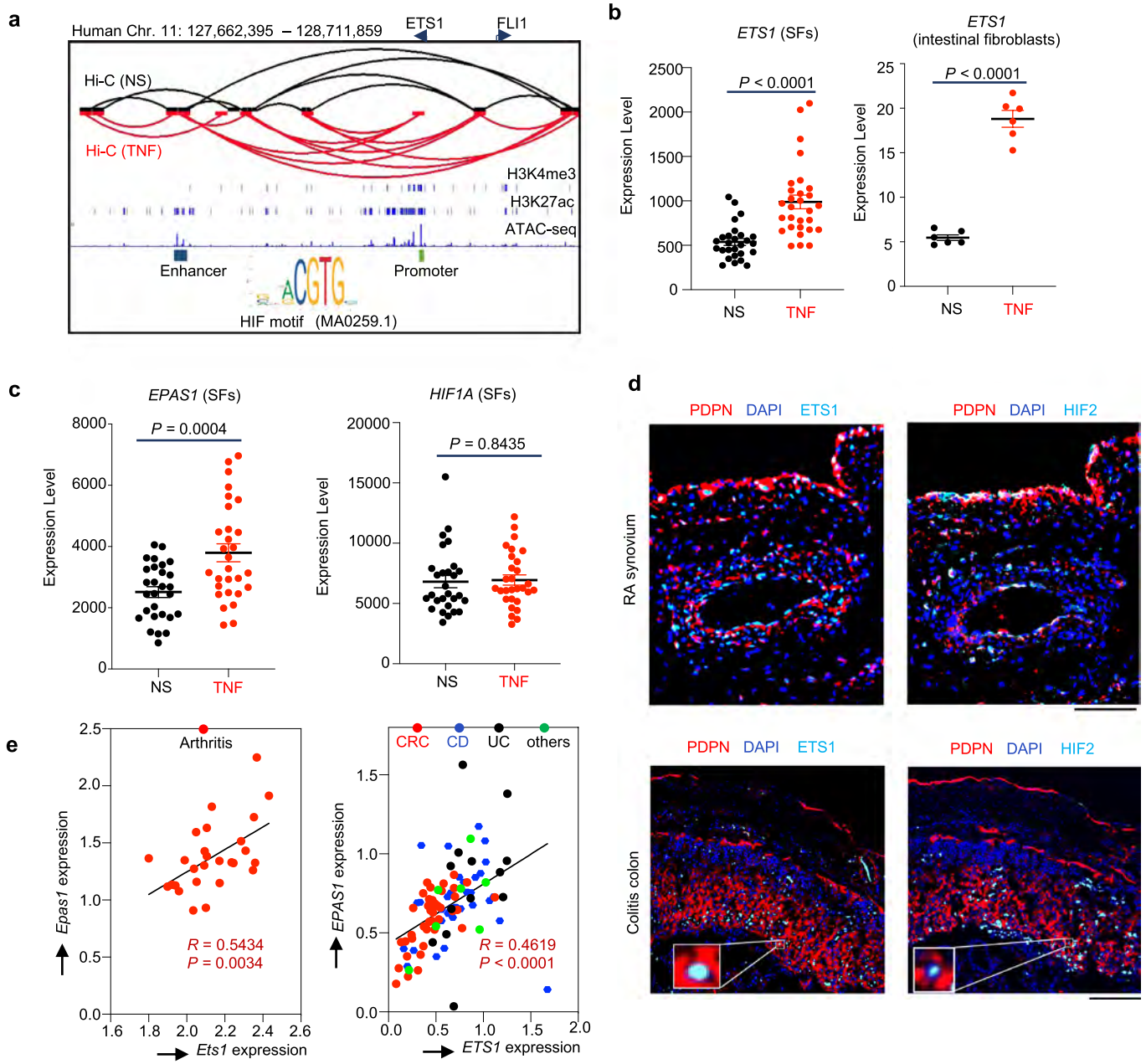

Extended Data Fig. 9 | Hypoxia may contribute to the ETS1 regulation in fibroblasts. a, Chromatin conformation and epigenomic analyses of SFs from RA patients at the *ETS1* locus (hg19) by Hi-C and H3K4me3, H3K27ac and ATAC-seq (NBDC accession code hum0207 and GSE128644). A loop-like structure appears between the *ETS1* promoter (open chromatin region with H3K4me3 signals) and enhancer region (open chromatin region with H3K27ac signals) under the condition (TNF stimulation) that could stimulate ETS1 expression in both synovial and intestinal fibroblasts (shown in (b)). The identified binding motif for hypoxia-inducible factor (HIF) (Jaspar, MA0259.1) was shown below. NS: no stimulation. b, The expression levels of ETS1 in SFs (NS, n = 28; TNF, n = 29) and intestinal fibroblasts (n = 6 per group) (NBDC accession code hum0207 and GSE166927). Data were expressed as mean ± s.e.m. *P* values were calculated by two-tailed *t*-test. c, The expression levels of *EPAS1* (NS, n = 28; TNF, n = 29) and *HIF1A* in SFs (NS, n = 28; TNF, n = 29) (NBDC accession code hum0207[24]). Data were expressed as mean ± s.e.m. *P* values were calculated by two-tailed *t*-test. d, Representative immunofluorescence images of RA synovium and inflamed colons, n = 2-3. Scale bars: 100 μm. e, Correlation analysis (Pearson r and two-tailed *P* value) between ETS1 expression and HIF2 (encoded by *EPAS1*) expression in arthritic SFs (n = 27) (GSE129451) and in tissues of colorectal cancer (CRC, n = 42), Crohn's disease (CD, n = 34) and ulcerative colitis (UC, n = 13) patients (GSE166925).

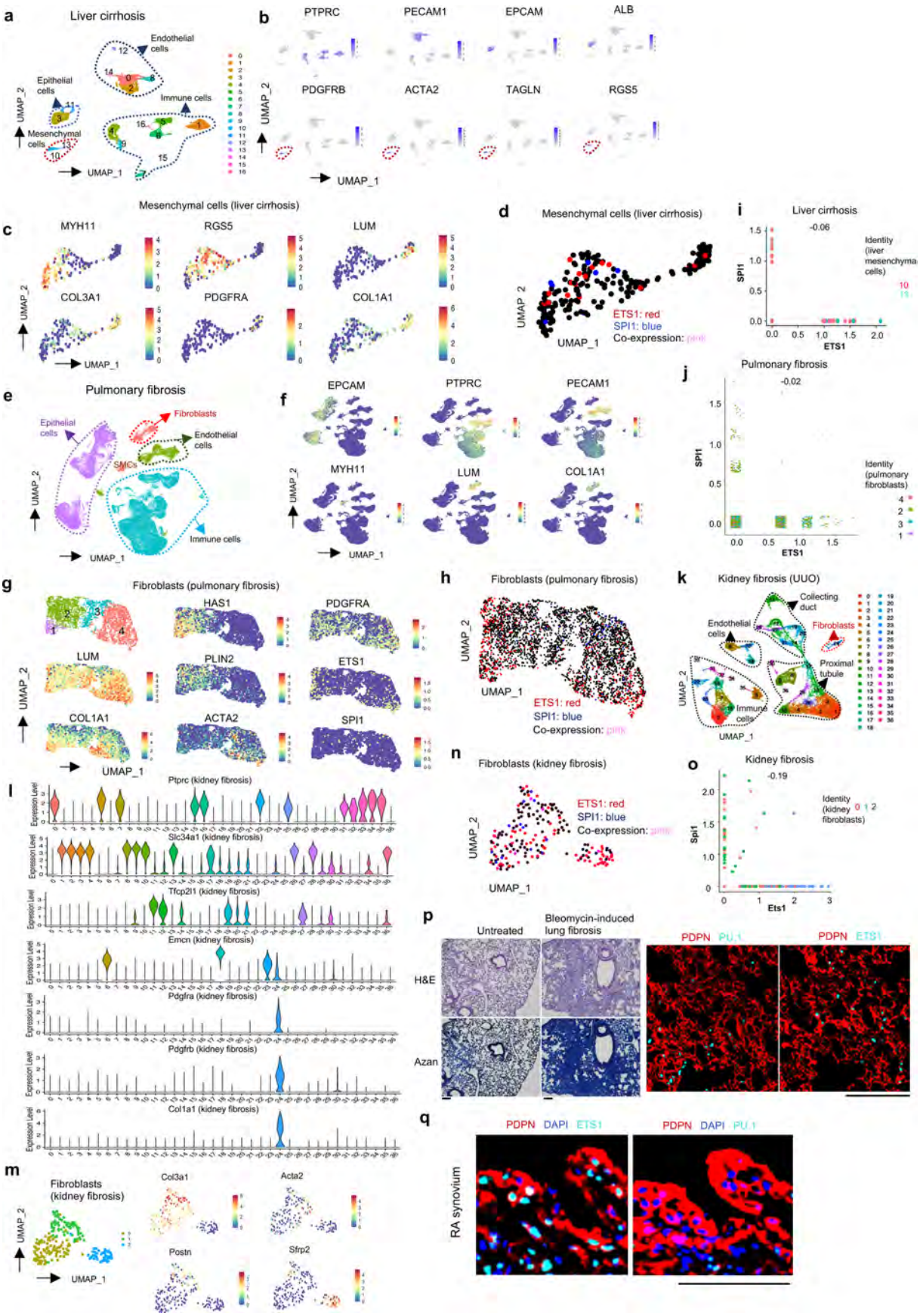

Extended Data Fig. 10 | See next page for caption.

Extended Data Fig. 10 | ETS1 and PU.1 expression in fibroblasts of fibrosis and arthritis. a, UMAP embedding of 6,898 cells derived from cirrhotic human livers (GSE136103) colored by cluster. b, Feature plot showing the expression of representative cell-type marker genes for cell type annotation in (a). c, d, The expression of representative genes (*MYH11, RGS5, LUM, COL3A1, PDGFRA, COL1A1*) (c) and *ETS1* (colored by red), *SPI1* (colored by blue) (d) in the identified mesenchymal cells (cluster 10 and cluster 13) of liver cirrhosis in the UMAP visualization. e, UMAP embedding of 119,438 cells derived from pulmonary fibrosis (GSE135893) colored by cell type. f, Feature plot showing the expression of representative cell-type marker genes for cell type annotation in (e). g, Unsupervised graph-based clustering of fibroblasts revealed four populations colored by cluster and the expression of selected genes in the UMAP visualization. h, The expression of *ETS1* (colored by red) and *SPI1* (colored by blue) in the fibroblasts of pulmonary fibrosis. i, j, A correlation between *ETS1* and *SPI1* expression in fibroblasts of liver cirrhosis (i) and pulmonary fibrosis (j). Each dot represents a single cell of the annotated clusters. k, UMAP embedding of 16,370 cells of unilateral-ureteric-obstruction (UUO)-induced kidney fibrosis (GSE140023) colored by cluster. l, Violin plots showing the expression of representative cell-type marker genes for cell type annotation in (k). m, Unsupervised graph-based clustering of fibroblasts revealed three populations colored by cluster and the expression of selected genes in the UMAP visualization. n, The expression of *Ets1* (colored by red) and *Spi1* (colored by blue) in the fibroblasts of kidney fibrosis. o, A correlation between *Ets1* and *Spi1* expression in fibroblasts of kidney fibrosis. Each dot represents a single cell of the annotated clusters. p, q, Representative H&E stained, Azan stained and immunofluorescence images of lung tissues of untreated, bleomycin-induced lung fibrosis model in mice (p) and RA synovium (q), n = 2-3. Scale bars: 100 μm.

nature portfolio

Corresponding author(s): Hiroshi Takayanagi

Last updated by author(s): Jul 7, 2022

Reporting Summary

Nature Portfolio wishes to improve the reproducibility of the work that we publish. This form provides structure for consistency and transparency in reporting. For further information on Nature Portfolio policies, see our Editorial Policies and the Editorial Policy Checklist.

Statistics

For all statistical analyses, confirm that the following items are present in the figure legend, table legend, main text, or Methods section.

n/a	Confirmed
☐	☒ The exact sample size (*n*) for each experimental group/condition, given as a discrete number and unit of measurement
☐	☒ A statement on whether measurements were taken from distinct samples or whether the same sample was measured repeatedly
☐	☒ The statistical test(s) used AND whether they are one- or two-sided *Only common tests should be described solely by name; describe more complex techniques in the Methods section.*
☐	☒ A description of all covariates tested
☐	☒ A description of any assumptions or corrections, such as tests of normality and adjustment for multiple comparisons
☐	☒ A full description of the statistical parameters including central tendency (e.g. means) or other basic estimates (e.g. regression coefficient) AND variation (e.g. standard deviation) or associated estimates of uncertainty (e.g. confidence intervals)
☐	☒ For null hypothesis testing, the test statistic (e.g. *F*, *t*, *r*) with confidence intervals, effect sizes, degrees of freedom and *P* value noted *Give P values as exact values whenever suitable.*
☒	☐ For Bayesian analysis, information on the choice of priors and Markov chain Monte Carlo settings
☒	☐ For hierarchical and complex designs, identification of the appropriate level for tests and full reporting of outcomes
☒	☐ Estimates of effect sizes (e.g. Cohen's *d*, Pearson's *r*), indicating how they were calculated

Our web collection on statistics for biologists contains articles on many of the points above.

Software and code

Policy information about availability of computer code

Data collection	Diva software (BD Biosciences, v9.0), BZ-II Analyzer (Biorevo BZ-9000, Keyence), Nikon C2 confocal microscope
Data analysis	GraphPad Prism v8.4.0 (GraphPad Software), FlowJo v10.6.2 (TreeStar), TRI/3D-BON software (RATOC), fastp v0.20.1, bowtie2 v2.3.5.1, MACS2 v2.2.7.1, Bedtools v2.29.2, IGV v2.7.0, HOMER v4.8, CellRanger v3.1.0, Seurat R packages (v3, v4), VISION v2.1.0, DESeq2 (v1.34.0), CLC Genomics Workbench (v12.0.3), pheatmap(v1.0.12), NIS-Elements AR v4.40.00 (Nikon), JASPAR 2020 (http://jaspar.genereg.net), ECR Browser (https://ecrbrowser.dcode.org/), LiftOver (https://genome.ucsc.edu/cgi-bin/hgLiftOver), cBioPortal (https://www.cbioportal.org), Single Cell PORTAL (https://singlecell.broadinstitute.org/single_cell), FibroXplorer (https://www.fibroxplorer.com), BioJupies (https://maayanlab.cloud/biojupies/analyze).

For manuscripts utilizing custom algorithms or software that are central to the research but not yet described in published literature, software must be made available to editors and reviewers. We strongly encourage code deposition in a community repository (e.g. GitHub). See the Nature Portfolio guidelines for submitting code & software for further information.

Data

Policy information about availability of data

All manuscripts must include a data availability statement. This statement should provide the following information, where applicable:

- Accession codes, unique identifiers, or web links for publicly available datasets
- A description of any restrictions on data availability
- For clinical datasets or third party data, please ensure that the statement adheres to our policy

All the data that support the plots within this paper and other findings of this study are available in the main text or the supplementary materials. The scRNA-seq

data and bulk RNA-seq data produced in this study were deposited to the public data base (GEO with the accession codes GSE192504 and GSE201310). The referenced publicly available data sets were downloaded from Gene Expression Omnibus (GEO), BioProject NCBI database, ENCODE Project database, The Cancer Genome Atlas (TCGA) database, National Bioscience Database Center (NBDC) database and MSigDB Collections C3 datasets: regulatory target gene sets (legacy transcription factor targets, https://www.gsea-msigdb.org/gsea/msigdb/index.jsp). Single cell RNA-seq (dbGaP Study Accession phs001529.v1.p1; ImmPort SDY998; GSE178341; SCP259; GSE176078; GSE136103; GSE135893; GSE140023; GSE172261), ChIP-seq (GSE128642; GSE148399; GSE54782; GSE123198; GSE145951; GSE155882; ENCODE: ENCFF614VLL; ENCFF982OBR, ENCFF577JGN, ENCFF169ARY, ENCFF244ZNY, ENCFF569PTY, ENCFF523ZCW, ENCFF213MVM, ENCFF383CFQ, ENCFF314JXH), ATAC-seq (GSE128644; BioProject PRJNA643827), Hi-C (NBDC hum0207), bulk RNA-seq (GSE129451; GSE148395; NBDC hum0207; GSE166927; GSE166925), TCGA clinical data and sequencing data (pancreatic adenocarcinoma (PanCancer Atlas), adult soft tissue sarcomas, mesothelioma (PanCancer Atlas), lung adenocarcinoma (Firehose Legacy), colon cancer CPTAC-2 Prospective and colorectal adenocarcinoma). R scripts for data analysis used in this study are available at GitHub (https://github.com/MingluYAN). Source data are provided with this paper.

Field-specific reporting

Please select the one below that is the best fit for your research. If you are not sure, read the appropriate sections before making your selection.

☒ Life sciences ☐ Behavioural & social sciences ☐ Ecological, evolutionary & environmental sciences

For a reference copy of the document with all sections, see nature.com/documents/nr-reporting-summary-flat.pdf

Life sciences study design

All studies must disclose on these points even when the disclosure is negative.

Sample size	No statistical method was used to predetermine the sample size. We chose the sample size based on our prior experience, and the standards in the relevant fields published in studies (Croft, A. P. et al., Nature, 570, 246-251, 2019; Wei, K. et al. Nature, 582, 259-264,2020) and remain in compliance with ethical guidelines to minimize the experimental animals.
Data exclusions	No data or samples were excluded from the analyses.
Replication	Experiments were successfully repeated at least once. The number of biological replicates (n) is reported for each experiment.
Randomization	Randomization was used whenever possible to determine the experimental order and groups. In the animal experiments, mice were randomly allocated for experiments. For the cell culture experiments, cells were randomly allocated to experimental groups.
Blinding	For the evaluation of the arthritis and disease activity of colitis, body weight loss, in vitro cell culture experiments and luciferase assays, researchers were not blinded since we analyzed the different genotype animals marked by ear cuts and the cells which were transfected with different plasmids. For the evaluation of histological scores and micro-CT analysis, investigators performed experiments in a blinded manner following the established workflow and instructions.

Reporting for specific materials, systems and methods

We require information from authors about some types of materials, experimental systems and methods used in many studies. Here, indicate whether each material, system or method listed is relevant to your study. If you are not sure if a list item applies to your research, read the appropriate section before selecting a response.

Materials & experimental systems

n/a	Involved in the study
☐	☒ Antibodies
☐	☒ Eukaryotic cell lines
☒	☐ Palaeontology and archaeology
☐	☒ Animals and other organisms
☐	☒ Human research participants
☒	☐ Clinical data
☒	☐ Dual use research of concern

Methods

n/a	Involved in the study
☒	☐ ChIP-seq
☐	☒ Flow cytometry
☒	☐ MRI-based neuroimaging

Antibodies

Antibodies used	Antibody/clone/catalog number/dilution Antibodies used for immunofluorescence staining: Rat anti-human Podoplanin antibody-PE/NC-08/BioLegend, Cat#337003/1:1000 dilution Rabbit ETS-1 antibody/D8O8A/Cell Signaling Technology, Cat#14069S/1:1000 dilution Rabbit PU.1 antibody/9G7/Cell Signaling Technology, Cat#2258/1:400 dilution Rabbit HIF-2 antibody/Novus Bio, Cat#NB100-122/1:200 dilution Syrian Hamster anti-mouse Podoplanin Antibody-APC/8.1.1/BioLegend, Cat#127410/1:200 dilution Rat anti-mouse CD326 (Ep-CAM) Antibody-PE/G8.8/BioLegend, Cat#118206/1:500 dilution

Donkey anti-rat IgG secondary antibody-Alexa Fluor 594/Invitrogen, Cat#A-21209/1:500 dilution
Donkey anti-rabbit IgG secondary antibody-Alexa Fluor 647/Invitrogen, Cat#A-31573, 1/500 dilution
Goat anti-Syrian hamster IgG secondary antibody-Alexa Fluor 647/Jackson ImmunoResearch, Cat#107-606-142/1:500 dilution
Goat anti-rabbit IgG secondary antibody-Alexa Fluor 488/Invitrogen, Cat#A-11034, 1:500 dilution

Antibodies used for Chromatin IP:
Rabbit ETS-1 antibody/D8O8A/Cell Signaling Technology, Cat#14069S, 1 ug/1ul
Normal rabbit IgG antiboby/Cell Signaling Technology, Cat#2729, 1 ug/ul

Antibodies used for lymphocyte stimulation
Purified anti-mouse CD3ε antibody/145-2C11/BioLegend, Cat#100301, 5 µg/mL
Purified anti-mouse CD28 antibody/37.51/BioLegend, Cat#102101, 1 µg/mL

Antibodies used for flow cytometry:
Human TruStain FcX (Fc Receptor Blocking Solution)/BioLegend, Cat#422301/1:100 dilution
Mouse anti-human CD45 antibody-Brilliant Violet 421/2D1/BioLegend, Cat#368521/1:100 dilution
Mouse anti-human CD31 antibody-PE-Cyanine7/WM59/BioLegend, Cat#303117/1:400 dilution
Mouse anti-human CD146 antibody-APC/P1H12/BioLegend, Cat#361015/1:400 dilution
Rat anti-human Podoplanin antibody-PE/NC-08/BioLegend, Cat#337003/1:100 dilution
Purified anti-mouse CD16/CD32 (2.4G2), TONBO Biosciences, Cat#70-0161-U100/1:100 dilution
Rat anti-mouse CD45 antibody-PerCP-Cyanine5.5/30-F11/BioLegend, Cat#103131/1:100 dilution
Armenian hamster anti-mouse CD3ε antibody-FITC/145-2C11/BioLegend, Cat#100305/1:100 dilution
Rat anti-mouse/human CD11b antibody-APC Cyanine7/M1/70/BioLegend, Cat#101225/1:400 dilution
Syrian hamster anti-mouse podoplanin antibody-PE-Cyanine7/8.1.1/BioLegend, Cat#127411/1:100 dilution)
Rat anti-mouse CD31 antibody-PE/390/BioLegend, Cat#102407/1:400 dilution
Rat anti-mouse CD146 antibody-APC/ME-9F1/BioLegend, Cat#134711/1:400 dilution
Rat anti-mouse CD90.2 antibody-Pacific Blue/53-2.1/BioLegend, Cat#140306/1:400 dilution
Armenian Hamster anti-mouse Notch3 antibody-PE/HMN3-133/BioLegend, Cat#130507/1:100 dilution
ETS1 recombinant rabbit monoclonal antibody/JM92-32/Invitrogen, Cat#MA5-32732/1:50 dilution
Goat anti-rabbit IgG secondary antibody-Alexa Fluor 488/Invitrogen, Cat#A-11034, 1:500 dilution

Validation

All the antibodies are commercially available, and we followed the statements of validation on the manufacture's website.
Rat anti-human Podoplanin antibody-PE/NC-08/BioLegend, https://www.biolegend.com/ja-jp/search-results/pe-anti-human-podoplanin-antibody-5798?GroupID=GROUP28
Rabbit ETS-1 antibody/D8O8A/Cell Signaling Technology, https://www.cellsignal.jp/products/primary-antibodies/ets-1-d8o8a-rabbit-mab/14069
Normal rabbit IgG antiboby/Cell Signaling Technology, https://www.cellsignal.jp/products/primary-antibodies/normal-rabbit-igg/2729
Rabbit PU.1 antibody/9G7/Cell Signaling Technology, https://www.cellsignal.jp/products/primary-antibodies/pu-1-9g7-rabbit-mab/2258
Rabbit HIF-2 antibody/Novus Bio, https://www.novusbio.com/products/hif-2-alpha-epas1-antibody_nb100-122
Syrian Hamster anti-mouse Podoplanin Antibody-APC/8.1.1/BioLegend, https://www.biolegend.com/ja-jp/products/apc-anti-mouse-podoplanin-antibody-6656
Rat anti-mouse CD326 (Ep-CAM) Antibody-PE/G8.8/BioLegend, https://www.biolegend.com/ja-jp/products/pe-anti-mouse-cd326-ep-cam-antibody-4726
Donkey anti-rat IgG secondary antibody-Alexa Fluor 594/Invitrogen, https://www.thermofisher.com/antibody/product/Donkey-anti-Rat-IgG-H-L-Highly-Cross-Adsorbed-Secondary-Antibody-Polyclonal/A-21209
Donkey anti-rabbit IgG secondary antibody-Alexa Fluor 647/Invitrogen, https://www.thermofisher.com/antibody/product/Donkey-anti-Rabbit-IgG-H-L-Highly-Cross-Adsorbed-Secondary-Antibody-Polyclonal/A-31573
Goat anti-Syrian hamster IgG secondary antibody-Alexa Fluor 647/Jackson ImmunoResearch, https://www.jacksonimmuno.com/catalog/products/107-606-142
Goat anti-rabbit IgG secondary antibody-Alexa Fluor 488/Invitrogen, https://www.thermofisher.com/antibody/product/Goat-anti-Rabbit-IgG-H-L-Highly-Cross-Adsorbed-Secondary-Antibody-Polyclonal/A-11034
Purified anti-mouse CD3ε antibody/145-2C11/BioLegend, https://www.biolegend.com/ja-jp/products/purified-anti-mouse-cd3epsilon-antibody-28
Purified anti-mouse CD28 antibody/37.51/BioLegend, https://www.biolegend.com/ja-jp/products/purified-anti-mouse-cd28-antibody-117
Human TruStain FcX (Fc Receptor Blocking Solution)/BioLegend, https://www.biolegend.com/ja-jp/products/human-trustain-fcx-fc-receptor-blocking-solution-6462
Mouse anti-human CD45 antibody-Brilliant Violet 421/2D1/BioLegend, https://www.biolegend.com/ja-jp/products/brilliant-violet-421-anti-human-cd45-antibody-14686
Mouse anti-human CD31 antibody-PE-Cyanine7/WM59/BioLegend, https://www.biolegend.com/ja-jp/search-results/pe-cyanine7-anti-human-cd31-antibody-6124?GroupID=BLG5721
Mouse anti-human CD146 antibody-APC/P1H12/BioLegend, https://www.biolegend.com/ja-jp/products/apc-anti-human-cd146-antibody-10412
Purified anti-mouse CD16/CD32 (2.4G2), TONBO Biosciences, https://tonbobio.com/products/purified-anti-mouse-cd16-cd32-2-4g2-fc-block
Rat anti-mouse CD45 antibody-PerCP-Cyanine5.5/30-F11/BioLegend, https://www.biolegend.com/ja-jp/products/percp-cyanine5-5-anti-mouse-cd45-antibody-4264
Armenian hamster anti-mouse CD3ε antibody-FITC/145-2C11/BioLegend, https://www.biolegend.com/ja-jp/products/fitc-anti-mouse-cd3epsilon-antibody-23
Rat anti-mouse/human CD11b antibody-APC Cyanine7/M1/70/BioLegend, https://www.biolegend.com/ja-jp/products/apc-cyanine7-anti-mouse-human-cd11b-antibody-3930
Syrian hamster anti-mouse podoplanin antibody-PE-Cyanine7/8.1.1/BioLegend, https://www.biolegend.com/ja-jp/products/pe-cyanine7-anti-mouse-podoplanin-antibody-6674
Rat anti-mouse CD31 antibody-PE/390/BioLegend, https://www.biolegend.com/ja-jp/products/pe-anti-mouse-cd31-antibody-122

Rat anti-mouse CD146 antibody-APC/ME-9F1/BioLegend, https://www.biolegend.com/ja-jp/search-results/apc-anti-mouse-cd146-antibody-9289?GroupID=BLG10622
Rat anti-mouse CD90.2 antibody-Pacific Blue/53-2.1/BioLegend, https://www.biolegend.com/ja-jp/punchout/search-results/pacific-blue-anti-mouse-cd90-2-thy-1-2-antibody-6762?GroupID=BLG8877
Armenian Hamster anti-mouse Notch3 antibody-PE/HMN3-133/BioLegend, https://www.biolegend.com/ja-jp/products/pe-anti-mouse-notch-3-antibody-5286
ETS1 recombinant rabbit monoclonal antibody/JM92-32/Invitrogen, https://www.thermofisher.com/antibody/product/ETS1-Antibody-clone-JM92-32-Recombinant-Monoclonal/MA5-32732
Goat anti-rabbit IgG secondary antibody-Alexa Fluor 488/Invitrogen, https://www.thermofisher.com/antibody/product/Goat-anti-Rabbit-IgG-H-L-Highly-Cross-Adsorbed-Secondary-Antibody-Polyclonal/A-11034

Eukaryotic cell lines

Policy information about cell lines

Cell line source(s)	293 T cells
Authentication	We checked the cell morphology and proliferation characteristics. We did not perform further authentication, since we did not draw conclusions specific to the 293T cell line.
Mycoplasma contamination	Cells were negative for mycoplasma contamination.
Commonly misidentified lines (See ICLAC register)	No commonly misidentified lines were used in this study.

Animals and other organisms

Policy information about studies involving animals; ARRIVE guidelines recommended for reporting animal research

Laboratory animals	C57BL/6 mice and DBA/1J mice were purchased from CLEA Japan and Charles River Laboratories Japan, respectively. Col6a1-Cre mice (Armaka, M. et al. J. Exp.Med. 205, 331-337, 2008) and Ets1flox mice (Kim, C. J. et al. Immunity 49, 1034-1048, 2018) were previously described. Fibroblast-specific Ets1-deficient mice (Ets1ΔFib) were generated by breeding Ets1flox mice with Col6a1-Cre mice. Enhancer KO mice (E1-KO, E2-KO, E3-KO) were generated by CRISPR/Cas9-mediated genome editing technology in this study. Single-guide (sg) RNA and Cas9 mRNA were described in the Method section. All the mice used in this study were 8- to 12-week-old, a mixture of both male and female mice except for DBA/1J mice (we use male DBA/1J mice for CIA experiments based on our experience)
Wild animals	No wild animals were used in this study.
Field-collected samples	The study did not involve wild animals.
Ethics oversight	Mice were maintained under specific pathogen-free conditions and all experiments were performed with the approval of the Institutional Review Board at The University of Tokyo. All the animals were maintained at a constant ambient temperature of 22-26 degree, 40-65% of humidity under a 12-hour light/dark cycle.

Note that full information on the approval of the study protocol must also be provided in the manuscript.

Human research participants

Policy information about studies involving human research participants

Population characteristics	We used human synovium tissue of RA patients (n=4, ranging 69-77 years old, male n=3, female n=1) in the immunohistochemistry and chromatin IP experiments,. All the subjects fulfilled the 2010 American College of Rheumatology-European League Against Rheumatism criteria for the classification for RA. Two patients were under the treatment of conventional synthetic disease-modifying anti-rheumatic drugs (csDMARDs) and the other two patients were treated with biologics at inclusion.
Recruitment	Human synovial tissue specimens were obtained from RA patients undergoing total knee joint replacement surgery at The University of Tokyo Hospital and provided written informed consent. There is no special bias or participant compensation in the sample recruitment.
Ethics oversight	Human subjects research was performed according to the Institutional Review Board at The University of Tokyo via approved protocols.

Note that full information on the approval of the study protocol must also be provided in the manuscript.

Flow Cytometry

Plots

Confirm that:

☒ The axis labels state the marker and fluorochrome used (e.g. CD4-FITC).

☒ The axis scales are clearly visible. Include numbers along axes only for bottom left plot of group (a 'group' is an analysis of identical markers).

☒ All plots are contour plots with outliers or pseudocolor plots.

☒ A numerical value for number of cells or percentage (with statistics) is provided.

Methodology

Sample preparation	Single-cell suspensions were prepared from the inflamed synovium tissue by enzymatic digestion using 4 mg/ml type II collagenase for 1 hour, and filtered by 100-µm cell strainers to remove the tissue debris. Erythrocytes were lysed using ACK Lysing Buffer and stained using Fc-blocker followed by specific antigens.
Instrument	Flow cytometry analysis and cell sorting were performed with FACS Canto II or FACS Aria III (BD Bioscience)
Software	FACS DIVA software (BD Bioscience, v9.0) and FlowJo v10.6.2 (TreeStar)
Cell population abundance	Cells were sorted at least more than 95% purity assessed by FACS Aria III
Gating strategy	Gating strategies were shown in the figures.

☒ Tick this box to confirm that a figure exemplifying the gating strategy is provided in the Supplementary Information.